Monthly Notices
of the
ROYAL ASTRONOMICAL SOCIETY

MNRAS 479, 435–453 (2018)
Advance Access publication 2018 May 31

doi:10.1093/mnras/sty1411

A bright-lensed galaxy at $z = 5.4$ with strong Ly α emission

Ian D. McGreer,[1,2★] Benjamin Clément,[3] Ramesh Mainali,[1] Daniel P. Stark,[1] Max Gronke,[4] Mark Dijkstra,[4] Xiaohui Fan,[1] Fuyan Bian,[5] Brenda Frye,[1] Linhua Jiang,[6] Jean-Paul Kneib,[7,8] Marceau Limousin[8] and Gregory Walth[9]

[1]*Steward Observatory, The University of Arizona, 933 North Cherry Avenue, Tucson, AZ 85721, USA*
[2]*Spaceflight Industries, 1505 Westlake Ave N Suite 600, Seattle, WA 98109, USA*
[3]*Univ Lyon, Univ Lyon1, Ens de Lyon, CNRS, Centre de Recherche Astrophysique de Lyon UMR5574, F-69230, Saint-Genis-Laval, France*
[4]*Institute of Theoretical Astrophysics, University of Oslo, Postboks 1029, 0315 Oslo, Norway*
[5]*Research School of Astronomy & Astrophysics, Australian National University, Canberra, ACT, 2611 Australia*
[6]*Kavli Institute for Astronomy and Astrophysics, Peking University, Beijing 100871, China*
[7]*Institute of Physics, Laboratory of Astrophysics, Ecole Polytechnique Fédérale de Lausanne (EPFL), Observatoire de Sauverny, 1290 Versoix, Switzerland*
[8]*Aix Marseille Univ, CNRS, CNES, LAM, Laboratoire d'Astrophysique de Marseille, Marseille, France*
[9]*University of California, Center for Astrophysics and Space Sciences, 9500 Gilman Drive, San Diego, CA 92093, USA*

Accepted 2018 May 25. Received 2018 May 25; in original form 2017 June 28

ABSTRACT

We present a detailed study of an unusually bright, lensed galaxy at $z = 5.424$ discovered within the CFHTLS imaging survey. With an observed flux of $i_{\rm AB} = 23.0$, J141446.82+544631.9 is one of the brightest galaxies known at $z > 5$. It is characterized by strong Ly α emission, reaching a peak in (observed) flux density of $>10^{-16}$ erg s^{-1} cm^{-2} Å^{-1}. A deep optical spectrum from the Large Binocular Telescope places strong constraints on N V and C IV emission, disfavouring an Active Galactic Nucleus (AGN) source for the emission. However, a detection of the N IV] λ1486 emission line indicates a hard ionizing continuum, possibly from hot, massive stars. Resolved imaging from *HST* deblends the galaxy from a foreground interloper; these observations include narrowband imaging of the Ly α emission, which is marginally resolved on approximately few kpc scales and has $\mathrm{EW}_0 \sim 260$ Å. The Ly α emission extends over $\sim$2000 km s^{-1} and is broadly consistent with expanding shell models. Spectral energy distribution fitting that includes *Spitzer*/IRAC photometry suggests a complex star formation history that includes both a recent burst and an evolved population. J1414+5446 lies 30 arcsec from the centre of a known lensing cluster in the CFHTLS; combined with the foreground contribution, this leads to a highly uncertain estimate for the lensing magnification in the range $5 \lesssim \mu \lesssim 25$. Because of its unusual brightness, J1414+5446 affords unique opportunities for detailed study of an individual galaxy near the epoch of re-ionization and a preview of what can be expected from upcoming wide-area surveys that will yield hundreds of similar objects.

Key words: (cosmology:) dark ages, re-ionization, first stars – galaxies: high-redshift – galaxies: individual: CFHTLS J141446.82+544631.9 – galaxies: ISM – galaxies: groups: individual: SL2S J141447+544703 – gravitational lensing: strong.

1 INTRODUCTION

The census of star-forming galaxies near the re-ionization epoch has expanded greatly in recent years, primarily due to deep imaging surveys at optical and near-infrared wavelengths that capture the rest frame ultraviolet emission produced by ongoing star formation (see review by Stark 2016). These surveys generally fall into two classes. Lyman Break Galaxies (LBGs) are colour-selected based on the sharp break in the continuum flux at the Ly α wavelength induced by the absorption of intervening neutral hydrogen at $z \gtrsim 4$. A subset of high-redshift galaxies is characterized by strong Ly α emission and are classified as Lyman-alpha Emitters (LAEs); they have traditionally been identified by the flux excess present in a narrow bandpass designed to capture the line emission, although powerful IFUs such as MUSE are increasingly being used to conduct line surveys (e.g. Smit et al. 2017). Deep surveys with the *Hubble Space Telescope* (*HST*) have been critical in building large samples of faint galaxies at $z > 5$, now numbering in thousands (Bouwens

★ E-mail: imcgreer@as.arizona.edu

et al. 2015), although extrapolation beyond the observed population is required for galaxies to provide sufficient ionizing photons to completely re-ionize the diffuse intergalactic gas (e.g. Robertson et al. 2015).

Broadly speaking, both LBG and LAE surveys at high redshift probe relatively small volumes. The most recent ultra-deep survey field from *HST* has an area of $<$5 arcmin^2 (UDF12: Ellis et al. 2013; Koekemoer et al. 2013); in total, the *HST* surveys have an area of $<$0.3 deg^2 (Bouwens et al. 2015). Recent ground-based surveys have yielded rarer, brighter LBGs in areas covering a few square degrees. (Willott et al. 2013; Bowler et al. 2015). LAE surveys can be successfully conducted from the ground as the narrow filter can be placed in regions of relatively low sky background between prominent OH sky emission bands (e.g. Kashikawa et al. 2004); the Hyper Suprime-Cam (HSC) surveys with the Subaru telescope are now probing LAEs at $z = 6$–7 over areas of tens of square degrees to exquisite depth (Ouchi et al. 2018). However, by employing a narrow bandpass, these surveys are restricted to thin redshift slices and hence relatively small volumes ($\sim$0.5 Gpc^3 for the HSC surveys). Blind spectroscopic surveys with slits or IFUs cover a much wider redshift range but are limited to small areas.

Because of the limited volume, galaxies discovered in the aforementioned surveys tend to be faint and difficult to study in detail. Bright galaxies can be examined with spectroscopic and multiwavelength observations, probing the physical conditions in individual systems (e.g. Bayliss et al. 2014; Yang et al. 2014; Smit et al. 2017) with tools otherwise limited to stacking analyses of large numbers of photometric galaxies (e.g. Jones, Stark & Ellis 2012). The profiles of both the Ly α emission line (e.g. Gronke, Bull & Dijkstra 2015) and interstellar absorption lines (e.g. Shapley et al. 2003) probe the covering fraction and kinematics of neutral gas, including large-scale outflows. Metal lines provide constraints on the ionizing radiation field in early galaxies, which may be driven by hard radiation from very hot, metal-poor massive star populations (Mainali et al. 2017; Stark et al. 2015a,b). Finally, mid-infrared photometry with the *Spitzer Space Telescope* constrains the stellar mass of bright galaxies and the presence of an evolved population of stars, indicating previous bursts of star formation.

We have discovered an extremely bright galaxy at $z = 5.426$ that was initially selected as a high-redshift quasar candidate. This object was drawn from a relatively wide-area imaging survey: the CFHTLS-W3 field (Gwyn 2012) covers 49 deg^2 to a depth of $i = 25.7$. With $i_{\rm AB} = 23.0$, it is (to the best of our knowledge) the brightest galaxy known at $z > 5$, with only a handful of galaxies even comparable in observed flux [e.g. the lensed galaxy A1689_2 at $z = 4.87$ has $I_{\rm AB} = 23.3$ (Frye, Broadhurst & Benítez 2002), the LAE J0335 at $z \sim 5.7$ has $I_{\rm AB} = 24.3$ (Yang et al. 2014)]. The galaxy, CFHTLS J141446.82+544631.9 (hereafter J1414+5446), is characterized by a strong Ly α emission line and a rare detection of N IV λ1468 emission. Whether it is *intrinsically* luminous is not clear, as its magnification due to gravitational lensing is poorly constrained.

The structure of the paper is as follows. First, in Section 2, we present an array of multiwavelength observations of the galaxy, including optical spectroscopy that confirms its redshift and characterizes the strong Ly α emission (Section 2.2 and Section 2.3); infrared photometry that probes the rest frame optical emission (Section 2.5); and both new and archival *HST* imaging that resolves the emission into multiple components (Section 2.4). Multiband image decomposition is used to characterize the observed morphology as detailed in Section 3. In Section 4, we explore the physical properties of this galaxy: the spatial extent of the UV continuum and Ly α emission; rest frame UV spectral properties including detailed modelling of the Ly α line profile; estimates of the gravitational lensing amplification from simulations of the foreground mass; stellar population models from spectral energy distribution (SED) fitting; and finally inferences about the star formation and ionizing spectrum. Brief conclusions are given in Section 5. All magnitudes are quoted on the AB system (Oke & Gunn 1983) and when needed a flat ΛCDM cosmology is adopted with parameters derived from the Planck 2013 results ($\Omega_\Lambda = 0.692$ and $H_0 = 67.8$ km s^{-1} Mpc^{-1}, Planck Collaboration et al. 2014a).

2 OBSERVATIONS

2.1 Initial selection from CFHTLS-W3

J1414+5446 was initially selected as a quasar candidate during our survey of faint $z \sim 5$ quasars in the CFHTLS imaging fields (McGreer et al. 2018). We started with the publicly available images and catalogues from the CFHTLS W3 field (Gwyn 2012), providing *ugriz* photometry over the 49-deg^2 field. We adopted the 2 arcsec aperture photometry measurements from the catalogues and then selected high-redshift quasar candidates using the Likelihood method outlined in Kirkpatrick et al. (2011) that assigns quasar probabilities based on the observed fluxes. Further details of our selection method can be found in McGreer et al. (2018).

J1414+5446 could also have been selected by simple colour criteria; e.g. the colour cuts we adopted in McGreer et al. (2013) to select $z = 5$ quasars. Although J1414+5446 proved to be a galaxy, we did not reject it as such using morphological criteria from the CFHT imaging. At this flux level star/galaxy separation is challenging; at the time J1414+5446 was targeted, we mainly eliminated galaxies by visual inspection of the images. Inspection of the CFHT images of J1414+5446 did not indicate that it was resolved; see Fig. 1.

J1414+5446 is covered by two independent pointings in the CFHTLS-W3 field (W3+0+0 and W3-0+0). During selection, we used the aperture photometry from a single field. We have since updated the photometry, first by using Point Spread Function (PSF)-shaped fluxes from PSFEx and second by co-adding the two sets of measurements. The improved CFHT photometry is provided in Table 1. The weak detections in the u and g bands are unexpected for a galaxy at this redshift. At the time of target selection, the significance of these detections was inconclusive and thus the object was not rejected as a high-redshift candidate. This issue will be discussed further in Section 3.1.

2.2 MMT observations

We first obtained a spectrum of J1414+5446 on UT 2012 May 28 using the Red Channel spectrograph on the MMT 6.5-m telescope. The object was placed in a 1 arcsec $\times$ 180 arcsec longslit after a blind offset from a nearby reference star and dispersed with a 270 mm^{-1} grating centred at 7500Å, providing coverage from 5700 Å to 9100 Å at a resolution of $R \sim$640. Two 20-min exposures in good conditions with 0.9 arcsec seeing were obtained.

The spectrum was reduced using standard IRAF tasks. Wavelength calibration was obtained from an HeNeAr lamp and then refined using night sky lines in the science spectra. Flux calibration was obtained from an observation of PG1708+602 taken shortly after the science observations.

We obtained a higher resolution spectrum of J1414+5446 on 2013 May 18 using the 1200–9000 grating on Red Channel. The spectrum extends from 7240 Å to 8050 Å at a dispersion of 0.8 Åpix^{-1}. We

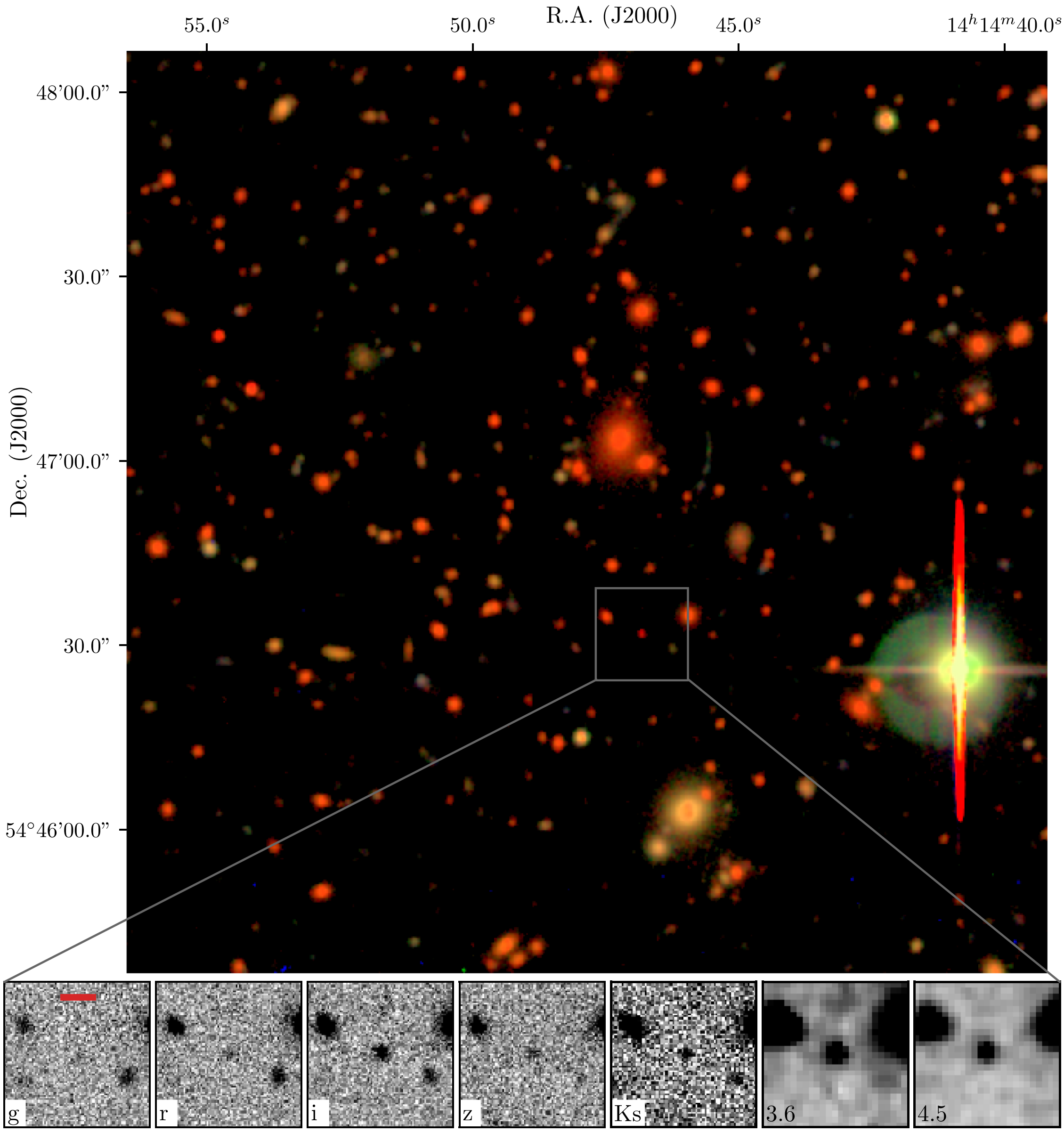

Figure 1. Colour image of the ∼2 arcmin field surrounding J1414+5446. The colour image is generated from the CFHT *gri* images using the Lupton et al. (2004) method. The brightest galaxy in the foreground group SL2S J141447+544703 (Cabanac et al. 2007) is clearly visible just above the image centre, as well as the large number of group member galaxies with similar colours. J1414+5446 lies just below the image centre, highlighted by the box. The panels in the bottom row display cutout images with a size of 15 arcsec from the CFHT *griz*, LBT/LUCI K_s, and Spitzer/IRAC 3.6-μm and 4.5-μm data (left to right). A 3 arcsec scalebar is provided in the leftmost panel (*g*-band) as a thick red line. J1414+5446 is not clearly resolved in any image, including the high-*S*/*N* *i*-band image that contains the Ly α emission.

measured a resolution of R ∼3000 at ∼7800 Å from unblended night sky lines. We obtained two exposures of 1800s each in ∼1.2 arcsec seeing at position angle (PA) of 157.6 deg. The spectra were processed with the same routines as for the low-dispersion spectrum, using observations of standard HZ44 for flux calibration. The flux calibration is highly uncertain, given the variable conditions during the observing period and the likelihood of slight mis-centreing of the object in the slit due to the use of a blind offset for acquisition.

2.3 LBT observations

In this section, we describe imaging and spectroscopy of J1414+5446 obtained with the 2 × 8.4-m Large Binocular Telescope (LBT). This includes optical imaging and medium-resolution spectroscopy with the MODS1 instrument (Pogge et al. 2006) and near-infrared imaging with the LUCI1 instrument (Seifert et al. 2003).

Table 1. Photometry of J1414+5446 based on total fluxes measured through elliptical apertures (SExtractor MAG_AUTO).

Source	Band	AB mag
CFHT	u	26.45 ± 0.28
	g	26.58 ± 0.23
	r	25.03 ± 0.08
	i	23.00 ± 0.02
	z	23.45 ± 0.09
LBT/MODS	g	26.61 ± 0.30
	i	22.89 ± 0.02
LBT/LUCI	J	23.77 ± 0.37
	K_s	23.14 ± 0.25
Spitzer	3.6 μm	22.37 ± 0.09
	4.5 μm	22.03 ± 0.06

Notes. Magnitudes are on the AB system (Oke & Gunn 1983) and have been corrected for extinction using the Schlegel, Finkbeiner & Davis (1998) maps. No attempt has been made to deblend the foreground and background galaxies.

2.3.1 LUCI1 imaging

We obtained J-band imaging with LUCI1 on 2013 March 5 in poor, non-photometric conditions with variable cloud extinction and ∼1.4 arcsec seeing. A total of 60 min of integration was accumulated through dithered 6 × 20 s individual exposures. Further LUCI1 observations were obtained on 2015 April 6–7 using the K_s bandpass. The night of 2015 April 6 was non-photometric with passing clouds with 0.7 arcsec seeing. The total exposure time was 36 min after rejecting a few integrations that were strongly affected by low transparency. The following night was photometric and the total exposure time was 44 min with seeing of 0.8 arcsec.

The LUCI1 data were processed in a standard fashion using IRAF tasks, incorporating dark current subtraction, flat-fields generated from combining the science images, and running sky subtraction. The processed images for each night were then shifted and combined to construct the final images. Individual images were weighted based on the transparency (T), seeing (FWHM), and sky background (B) as T/(FWHM^2 + B) when combining, where each weight term is relative to the maximum value of the given parameter. Finally, the combined images were binned by a factor of 2 along each axis to a resulting pixel scale of 0.24 arcsec. Object detection was performed on the binned images using SExtractor (Bertin & Arnouts 1996), and astrometric solutions were obtained by matching well-detected objects to the CFHTLS-W3 i-band catalogue.

We used 2MASS (Skrutskie et al. 2006) stars detected within the field to determine the image zero points. The calibration accuracy is severely limited by the small number of 2MASS stars available – only 5 (2) in the J (K_s) band. We checked the LUCI photometry against red sequence galaxies selected from the images, most of which lie at the foreground cluster redshift. Comparing our colours to a template red galaxy spectrum at this redshift, we find shifts of ∼0.25 and ∼0.13 mag in the J and K_s bands, respectively. We apply these shifts and add an equal amount of error in quadrature to the photometry in order to capture the calibration uncertainty.

2.3.2 MODS1 imaging

We observed J1414+5446 with the imaging mode of MODS1 on 2014 May 31. MODS1 includes a dichroic for observing blue and red wavelengths simultaneously. The field-of-view in the 3K × 3K imaging mode is 6 arcmin across, and the pixel scale for the blue (red) channel is 0$''$.120 (0$''$.123). We used the g filter in the blue channel and the i filter in the red channel and obtained six dithered exposures with individual integration times of 5 min. Conditions were clear and photometric, and the seeing measured from the images is 0$''$.6 in the i band and 0$''$.75 in the g band.

Standard methods were employed to process the optical images, using custom Python routines. A series of bias images were median-combined to create a master bias. Pixel flat-fields were generated from a series of exposures taken with an internal lamp. The final flat-field correction consisted of a stack of the pixel flats, as well as an illumination correction derived from twilight sky flat images. After applying the bias and flat-field corrections, the individual science images were processed and combined using Scamp (Bertin 2006) to obtain initial astrometric solutions and SWarp (Bertin et al. 2002) to co-add the images. Sky subtraction was enabled when combining with SWarp as the sky level varied substantially over the course of the observations. The images were combined in two iterations; the first iteration produced a reference image from which cosmic rays and other defects in individual images were identified and masked prior to the final co-addition.

We produced two sets of final images in each band. The first are in the native pixel scale and footprint of each detector. The second are matched to the g-band pixel scale and aligned using SWarp. We derive object catalogues from all images using SExtractor; for the pair of aligned images, we used dual-image mode with the i-band image for detection. Finally, we registered the images to the CFHTLS astrometry and determined the photometric zero point by matching to stars in the CFHTLS catalogues. The MODS g and i filters are slightly bluer than the corresponding CFHT filters; we thus corrected for a slight tilt ($\lesssim$1 per cent over the range of interest) between the two photometric systems in order to place the LBT magnitudes on the CFHT system. The calibrated photometry from the dual-image mode catalogues is listed in Table 1 and postage stamp images are displayed in Fig. 2. The primary result from this imaging is confirmation of the g-band detection in the CFHTLS.

Table 2. LBT/MODS1 multislit spectroscopic observations. The final column notes which of the lensed arc candidates described in Section 2.3.3 are included on each mask.

Mask ID	UT	Exp. (h)	Conditions	Notes
505919	2013-04-13	1.9	0.8 arcsec, passing clouds	T1
523405	2015-03-25	3.8	1.0 arcsec, clear	T1
510122	2015-03-26	3.7	0.6–1.0 arcsec, cloudy	R1, R2

2.3.3 MODS1 spectroscopy

We obtained optical spectroscopy of J1414+5446 with MODS1 on three different nights. The goals of the spectroscopy were twofold. First, to obtain a deep spectrum of the high-z galaxy to search for weak emission and absorption features. Secondly, we targeted the lensed arc candidates as well as cluster member galaxies in order to better constrain the lensing model. We designed three slitmasks, each of which included the J1414+5446 as a target. Two of the masks included slits for a long tangential arc (T1 in Cabanac et al. 2007) and one mask included both of the candidate radial arcs (R1 and R2 in More et al. 2012). Details of the MODS1 observations are provided in Table 2 and results from the multiobject spectroscopy are described in Appendix A.

All observations employed the dual grating mode of MODS1 for complete wavelength coverage from 3200 Å to 1 μm. The slits for J1414+5446 were 14–20 arcsec in length while the slits for the

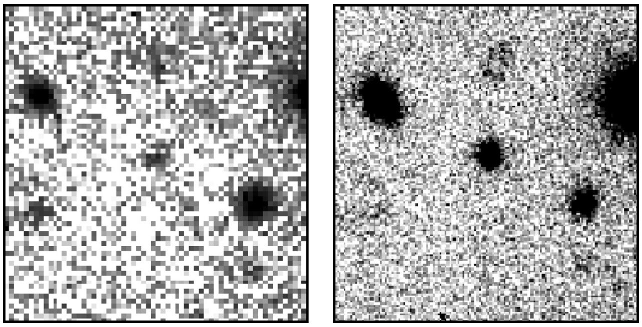

Figure 2. LBT/MODS1 g- and i-band image cutouts of J1414+5446, with the same orientation as in Fig.1. The g-band image has been re-binned by a factor of 2 and is displayed on an arcsinh scale to enhance the weak detection of J1414+5446. Although faint, this clearly confirms the $\sim 2\sigma$ flux measured from the CFHT image. The i-band image is displayed at native resolution; J1414+5446 is detected at high S/N and is unresolved in 0.″6 seeing.

galaxy targets were 7–10 arcsec; all slits had a width of 1 arcsec. The resolution in the blue channel (up to 6000 Å) is $R \sim 1100$ and in the red channel (starting at 5000 Å) is ∼1400.

modsidlmodsccdredThe spectra were processed with Version 2.0 of the software, and version 0.2p1 of the modsidl spectral reduction pipeline.[1] Individual frames were bias-subtracted and then flat-fielded using a series of internal lamp calibrations. Wavelength calibration was provided by a combination of internal arcs and has an rms <0.1Å. Flux calibration was obtained through observations of the spectrophotometric standard stars Feige 34 and BD+33d2642 acquired in the same night. The individual science frames were sky-subtracted and 1D spectra were extracted using . The modsidl implementation uses boxcar extraction; we constructed model profiles using stars included in the slit masks and used these models to perform optimal extraction (Horne 1986), with a significant gain in S/N compared to the boxcar-extracted spectra. The individual spectra from each night were combined with inverse-variance weighting, scaling the Ly α flux measured from each image to account for transparency variations. Finally, the spectra from the three nights were combined to produce the final MODS spectrum shown in Fig. 3. Before combining, a correction to the flux calibration for the spectra from each mask was determined by comparing the spectrophotometry obtained for the field galaxies to their photometry in the CFHTLS. The total exposure time is ∼9.4 h; however, two of the nights were affected by passing clouds and we estimate the effective exposure time to be ∼7 h.

2.4 *HST* imaging

2.4.1 Archival WFPC2 observations

J1414+5446 is within the field of SL2S J141447+544703, a lensing group included in the Strong Lensing Legacy Survey (SL2S; Cabanac et al. 2007). This survey identified candidate strong lenses up to $z \sim 1$ in the CFHTLS imaging and included *HST* observations as part of a Cycle 16 SNAPSHOT program (GO #11289, PI: Kneib). The SL2S J141447+544703 field was observed with three dithered 400 s exposures using the WFPC2 instrument and the F606W bandpass. J1414+5446 is located ∼30 arcsec from the centre of the lensing group and was well within the WFCP2 image. The F606W bandpass is entirely blueward of Ly α at $z = 5.4$ and thus samples the attenuated rest-FUV continuum of the galaxy.

We processed the archival WFPC2 images using ASTRODRIZZLE ,[2] setting pixfrac = 1.0 and drizzling to a final pixel scale of 0.″05. We found that the default astrometry matched the CFHT astrometry to an accuracy of <0.″05 . J1414+5446 is clearly detected in the final WFPC2 mosaic; furthermore, on <0.″4 scales, it resolves into up to four components (Fig. 4).

2.4.2 Cycle 22 ACS/WFC3 observations

We obtained Cycle 22 imaging of J1414+5446 on 2015 November 14 with ACS and WFC3 (GO #13762, PI: McGreer). We employed three bandpasses to probe the rest-UV continuum from the high-z galaxy: ACS/F850LP and WFC3-IR F125W and F160W, spanning ∼1400–2600 Å rest frame. We also used the ACS ramp filter FR782N centred at 7816Å to capture the Ly α emission. The total exposure times were 813 s for the ramp filter, 1011 s for ACS/F850LP, and 1359 s each for the two WFC3 bands. All observations used a standard three-point dither pattern. We imposed an orientation constraint on the ACS observations to ensure that the F850LP image would include the brightest cluster galaxy (BCG) and the lensed arcs.

Images were processed using ASTRODRIZZLE. A first-pass drizzled ACS/F850LP image was registered to the CFHT i-band astrometry as with the WFPC2 image. The F850LP and FR782N images were obtained in the same orbit with the same orientation and field centre, thus the updated astrometry was propagated back into all the ACS images using the TWEAKSHIFTS routine before generating a final mosaic. We used pixfrac = 0.8 and a scale of 0.″03 for the output pixel grid (Koekemoer et al. 2011). The WFC3 images were processed in a similar fashion but with a final scale of 0.″06. Comparing object centroids between the various *HST* bands, we find that they are aligned to $\lesssim$0.″05 accuracy.

We generated empirical PSF models for the broadband images from stars within the field using IRAF DAOPHOT tasks. The narrowband image has only a single-stellar object with sufficient signal-to-noise to serve as a PSF reference. J1414+5446 is well detected in all *HST* images, including the narrowband (Fig. 4). We will discuss multicomponent fits to the *HST* images in Section 3.2.

2.5 Spitzer Cycle 9 observations

Mid-IR observations have a key role in characterizing high redshift galaxies by providing constraints on the SED redward of the Balmer break. Compared to rest-UV wavelengths, rest frame optical observations better probe the star formation history, stellar mass, and dust extinction, and thus are essential to forming a more complete picture of the stellar population.

J1414+5446 was observed with the IRAC camera on Spitzer during the Warm Mission (GO #90195, PI: McGreer). The observations consisted of a single Astronomical Observation Request with integrations in the 3.6-μm and 4.5-μm channels totalling 1800 s in each channel using a standard dither pattern. We estimate a point source sensitivity of ∼1.5 μJy (5 σ) from both the 3.6-μm and 4.5-μm images. J1414+5446 is clearly detected in both images, with total fluxes of $f_{3.6} = (4.08 \pm 0.33)$ μJy and $f_{4.5} = (5.58 \pm 0.30)$ μJy measured through aperture photometry (SExtractor MAG_AUTO).

[1] http://www.astronomy.ohio-state.edu/MODS/Software/modsIDL/

[2] http://drizzlepac.stsci.edu/

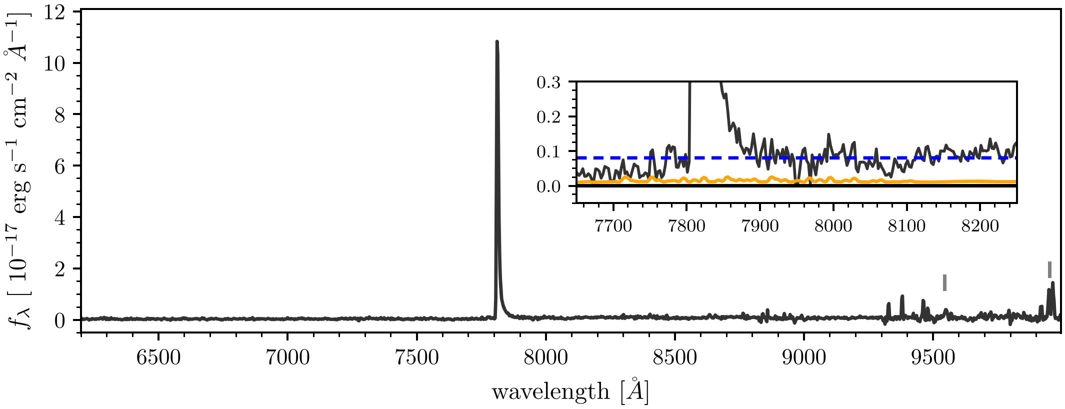

Figure 3. LBT/MODS1 spectrum of J1414+5446, dominated by the strong Ly α emission feature. The inset panel highlights the continuum emission detected at $\sim 2\sigma\,\mathrm{pix}^{-1}$ redward of the Ly α emission (the continuum fit is indicated by the dashed blue line and the error spectrum by the solid orange line). Flux is also detected at $\sim 1\sigma\,\mathrm{pix}^{-1}$ blueward of Ly α, although there is a clear spectral break at the wavelength Ly α. The wavelengths of the N IV and C IV features are marked with small vertical lines and will be discussed in Section 4.2.

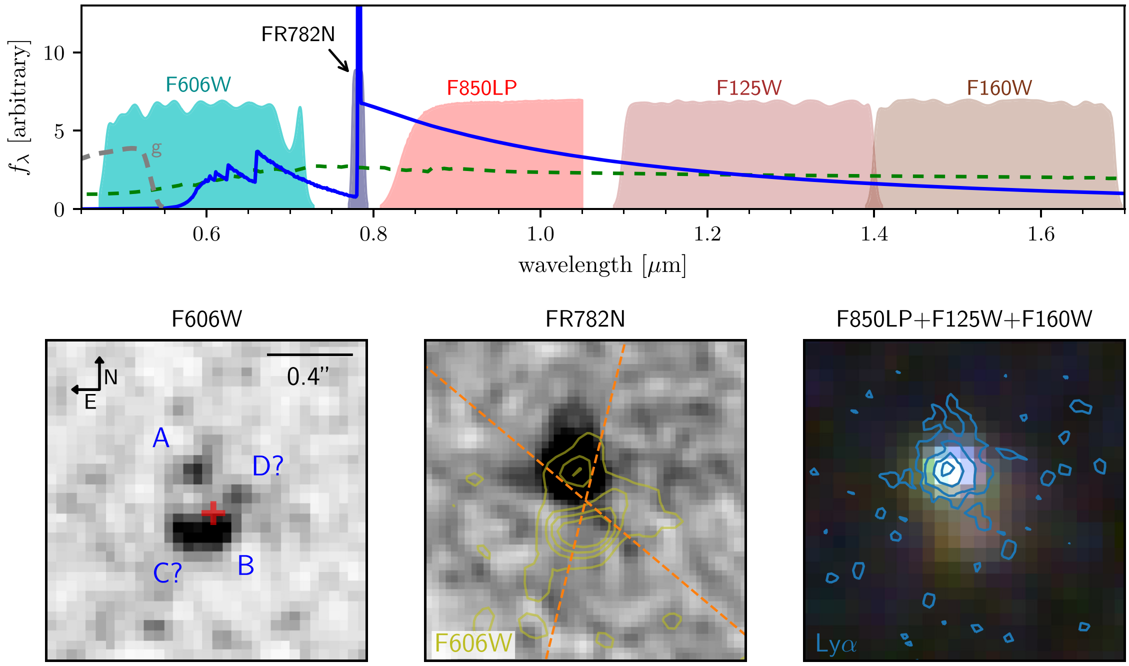

Figure 4. *HST* imaging of J1414+5446. The top panel displays the filter set, including the ACS ramp filter used for narrowband imaging of Ly α (FR782N). A model for the LAE spectrum based on its observed properties is represented by a blue line, while an Sbc template for the foreground galaxy is represented by a green dashed line. The bottom three panels present the *HST* images, oriented as indicated in the lower left panel. The F606W image clearly has multiple components. The labels match those in Table 3. Labels C and D mark low-significance peaks in the *HST* image that are putative detections; in the analysis, C is modelled as both a separate component and as part of B, while D is ignored. The red plus sign marks the location of the g-band centroid obtained from the CFHT/LBT imaging. The middle panel presents the narrowband image, smoothed with a 1-pixel Gaussian and overlaid with linearly spaced contours from the F606W image. The approximate locations of the spectroscopic slits for the two MODS masks are indicated with dashed orange lines. The right-hand panel presents a colour composite constructed from the ACS and WFC3 images, where the ACS image has been convolved with a Gaussian and resampled to match the WFC3 PSF and footprint. Logarithmically spaced contours from the narrowband (Ly α) image are overlaid in cyan lines.

3 IMAGE MODELLING

3.1 Foreground galaxy

The g-band detections, and marginal u-band detection, are somewhat puzzling. Both bands are completely blueward of the Lyman Limit at this redshift (see Fig. 4) and thus will be subject to Lyman continuum absorption. The co-moving mean free path of Lyman Limit photons at $z = 5.4$ is $\sim 60 h_{70}^{-1}$ Mpc (Worseck et al. 2014); hence, the probability that significant flux would transmit through the intergalactic medium (IGM) from a high-redshift galaxy into these bands is exceedingly low. We used Monte Carlo simulations[3]

[3]The simulations are described in greater detail in McGreer et al. (2013) and are based on the forest model of Worseck & Prochaska (2011), extended to include the incidence of high-redshift Lyman Limit Systems from Songaila & Cowie (2010).

of Ly α forest transmission spectra at $z = 5.4$ to examine the possibility that an IGM sightline would be sufficiently transparent to allow detectable g-band flux from J1414+5446. After generating a model galaxy spectrum based on the photometry at longer wavelengths (conservatively assuming a blue UV slope of $\beta_\lambda = -1.5$ and an escape fraction of unity), we find that none of the 2000 simulated sightlines had $g < 28$, compared to the measured fluxes of $\sim$26.5. We conclude that the flux at blue wavelengths must be due to a foreground interloper.

An interesting question is whether the interloper would have impeded selection of the high redshift galaxy according to standard colour selection methods. The criteria employed for our quasar selection are very similar to those used to select 'dropout' galaxies. As noted previously, we did not reject this object as the g-band photometry in the catalogues we used for selection reported a $<$2.5 σ detection. However, a stricter cut on the bluer bands may have rejected this object. In addition, the faint fluxes in the bluer bands are sufficient to affect photometric redshift estimation. The CFHTLS photometric redshift catalogues of Ilbert et al. (2006) and Coupon et al. (2009) place J1414+5446 at $z = 0.75$, with a 68 per cent confidence interval of $0.68 < z < 0.89$. The fluxes in the blue optical bands result in this high-redshift galaxy having roughly similar colours to the red galaxies at the cluster redshift, and thus it could be easily overlooked by broadband colour selection.

3.2 *HST* image decomposition

Interpretation of the high-resolution images from *HST* is not straightforward. The WFPC2 F606W image (Fig. 4) shows the largest degree of apparent structure, with up to four individual emission peaks. On the other hand, the narrowband image has only a single prominent source. The F850LP image is dominated by a bright source that coincides with the narrowband detection, with the addition of a faint source to the SW. The WFC3 images appear to have two components of roughly equal strength, roughly matching the morphology of the F850LP image.

It is not obvious how to associate individual components across all of the emission bands. The narrow band image pinpoints the location of the Ly α emission from the $z = 5.4$ galaxy. Emission peaks at this position are present in all bands, including F606W (see the component labelled 'A' in Fig. 4). On the other hand, the foreground galaxy should dominate the g-band emission. The centroid obtained from the ground-based CFHT/LBT g-band imaging most closely aligns with the brightest component found in the F606W image (labeled B in Fig. 4). This position is also well matched to the extended emission to the SW of the Ly α peak in the *HST* images.

We implemented a multiband-fitting procedure in python that allows for an arbitrary number of point source (hereafter PSF) and extended object components to be included in a given model. These components are then rendered into images for each *HST* band by convolving the model with empirical PSFs derived from field stars. The extended components are based on Sérsic profiles. The rendered images are then compared to the data with a χ^2 statistic, summing the contributions from all bands. A minimization routine (the Nelder–Mead gradient search implemented in Scipy) is then used to find the best-fitting set of parameters. During this procedure, we exclude the narrowband image as it probes only the Ly α emission from the high-z galaxy, which may have a different morphology than the continuum emission.

We then experimented with a number of configurations to fit the individual emission components in the *HST* images. Unresolved components are modelled with three parameters (x, y, and flux),

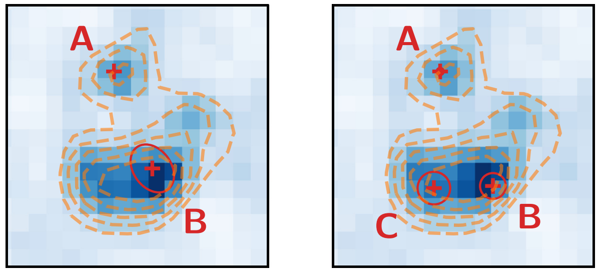

Figure 5. Image models for the two (left-hand panel) and three (right-hand panel) component fits to the *HST* images. The background image is from WFPC2/F606W, with a pixel scale of 0.05 arcsec. The dashed lines are linearly spaced surface brightness contours from the F606W image. Positions of the individual components are labelled and marked with plus signs. Extended components (Sérsic profiles) are represented with an ellipse based on the fitted parameters (displayed without PSF convolution), with a radius of $r_{\rm eff}/5$. The size of the image cutouts is 0.4 arcsec and the orientation is N through E, as in Fig. 4.

while Sérsic profiles have a total of seven parameters (x, y, flux, effective radius, Sérsic index, ellipticity, and PA). Given the large number of parameters and the substantial blending apparent in the images (leading to degeneracies in the fits), we reduce the number of parameters by making some simplifying assumptions. We fixed the position of the Ly α-emitting component (A) to the position obtained from the F850LP image, where it is cleanly detected at high significance. We required the positions of any additional Sérsic components to be identical across all bands. Finally, we found that fitting the sky background was unnecessary and thus simply removed a median value from each band using nearby sky pixels.

Our fiducial configuration (left-hand panel of Fig. 5) consists of a single PSF component (A) aligned with the bright source in the F850LP image, and a Sérsic component (B). We required the PA of the Sérsic component to be identical in all bands and fixed the index to $n = 1.1$ and the ellipticity to 0.28 in all bands. The latter values were found by allowing those two parameters to vary while holding other parameters fixed. The effective radius is allowed to vary between bands in order to account for morphological variations with wavelength. This model provides a reasonably good fit to the data, with $\chi^2_\nu = 1.22(16377/13426)$. The best-fitting effective radius is 0.7 arcsec $\pm$ 0.1 arcsec in the F606W band and 0.9 arcsec $\pm$ 0.03 arcsec in the other bands. In this model, we assume that the PSF component corresponds to all of the flux from the high-z galaxy, and the Sérsic component is contributed entirely by a low-z interloper.

In the F606W image, the SW component is highly asymmetric, with a strong peak and extended emission to the east. We consider the possibility that this emission represents a separate component by constructing a model with three components, where all components are represented by Sérsic profiles (right-hand panel of Fig. 5). The initial positions and fluxes were obtained from simple Gaussian fits to the individual peaks in the F606W image. We fixed the positions of all components to their initial positions and also fixed the Sérsic profiles to have zero ellipticity and required that the effective radii and Sérsic indices were identical across all bands. Although the Ly α-emitting component is modelled with a Sérsic profile rather than a PSF as before, the best-fitting effective radius is $\sim$0.1 arcsec, indicating that the source is at best marginally resolved in the broadband images. Components B and C both have

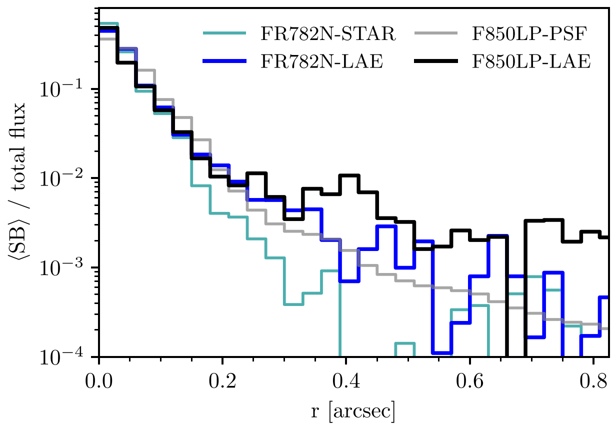

Figure 6. Radial profiles of the Ly α (FR782N) and UV continuum (F850LP) emission, expressed as the average surface brightness of pixels within radial annuli of width 0.″03, normalized by the total flux in a 1.2-arcsec aperture. The profile from the PSF derived for the F850LP image is marked a light grey line, while the LAE profile is black. The profile from the single reference star in the narrowband image is shown in light blue, while the LAE profile is dark blue. Errors on the radial profiles are typically smaller than the line width and not displayed.

$r_e \approx 0.4$ arcsec and the best-fitting Sérsic indices are rather flat ($n \lesssim 1$). The fit is improved compared to the two-component model: $\chi^2_\nu = 1.20(16060/13423)$. The addition of three parameters is statistically significant according to the Aikake Information Criteria (ΔAIC $\approx$ 300). However, splitting the fluxes between the B and C components results in large photometric uncertainties, thus it is difficult to reliably constrain the contribution from each component.

Furthermore, the three-component fit has more ambiguity in its interpretation. Associating component B with the foreground galaxy remains clear, but the second component (C) could either be in the foreground or at high-z, i.e. it could be continuum emission from the high-z galaxy without associated Ly α emission, as is often observed (Jiang et al. 2013; Pirzkal et al. 2007; Venemans et al. 2005). We consider the latter interpretation to be less likely, as this would imply relatively bright emission in a very blue band ($V_{606} \approx 25.9$) along with relatively faint emission in the rest-UV continuum ($J_{125} \approx 25.9$), compared to $V_{606} = 27.7$ and $Y_{125} = 23.7$ for the Ly α-emitting component. In order to be more conservative, we adopt the two-component model to interpret the *HST* data.

3.3 Narrowband Ly α imaging

The ACS/FR782N band was selected to map the spatial extent of the Ly α emission from the $z = 5.4$ galaxy with the resolution available from *HST*. The bandwidth of the ramp filter is ∼150 Å, fully encompassing the extent of the Ly α emission from spectroscopy (∼70 Å, Fig. 3). The narrowband image is presented in Fig. 4. As discussed in the previous section, the single narrowband detection is also well detected in the broadbands redward of the Ly α line. Fitting a power law to the F850LP, F125W, and F160W measurements (Table 3), we obtain a slope of $\beta_\lambda = -2.58 \pm 0.03$.

The total flux in the narrowband is $m_{782} = 20.79 \pm 0.04$ as measured through a 0.″8 aperture. Extrapolating the continuum fit to this wavelength results in EW$_0$ = 260 ± 12Å. One of the key aims of the *HST* program was to obtain resolved photometry of the rest-UV emission, removing the foreground contamination. As described in Section 4.2, the EW of the Ly α emission obtained from ground-based spectroscopy is consistent with the value from the *HST* narrowband imaging once the foreground contamination is taken into account. Thus, the large EW is robust and is slightly greater than the limit generally assumed for emission from normal stellar populations (240 Å, e.g. Charlot & Fall 1993; Schaerer 2002), although objects with similarly large Ly α EWs have been discovered in large narrowband surveys (e.g. Hashimoto et al. 2017; Shibuya et al. 2018).

The narrowband image contains a single-stellar object with sufficient *S/N* to characterize the PSF. Comparing the radial profile of this object to the J1414+5446 detection, the latter is clearly more extended (Fig. 6). For the star, 90 per cent of the total flux is contained within a 0.″15 radius, while for the LAE, this radius is 0.″45. The Ly α flux extends to 0.″6 in this relatively shallow image (the surface brightness limit is ∼22.3 mag arcsec^{-2}). Note that component B is separated from the LAE by ∼0.4 arcsec and contributes a small amount of flux to the F850LP profile; however, it is undetected in the narrowband image. Several faint features appear to extend outwards from the central source after smoothing the narrowband image, although they are weak and do not permit a detailed morphological analysis.

In general, the lack of (or very weak) extended Ly α emission is in contrast to some recent work that finds extended Ly α haloes around high-redshift galaxies with strong Ly α emission, with the line emission extending over a region 5–10× greater than the continuum emission (e.g. Wisotzki et al. 2016; Smit et al. 2017). J1414+5446 may lack the conditions required for such a halo to form. Alternatively, the central region may be in a region of higher lensing magnification compared to the more extended halo (see Section 4.5 for discussion of the lensing properties).

4 PHYSICAL PROPERTIES OF THE GALAXY

4.1 Spatial extent

From the analysis of the *HST* imaging presented in Section 3, we conclude that both the UV continuum and Ly α emission from J1414+5446 are at best marginally resolved. Both show slight excess emission out to ∼0.″6 (Fig. 6); however, it is difficult to draw robust conclusions on any differences between the UV continuum and Ly α morphology from the available images.

4.2 Rest frame UV spectra

J1414+5446 is exceptionally bright at optical wavelengths and provides a unique opportunity to probe the physical conditions in a high-redshift galaxy using typical diagnostic tools applied to rest frame UV spectra. The ∼9-h LBT spectrum achieves an *S/N* of ∼3 in the rest-UV continuum (∼1250 Å) and can be used to explore key emission and absorption features at these wavelengths.

The foreground interloper complicates the interpretation of the LBT spectrum. Fortunately, the *HST* imaging constrains the expected UV continuum from the LAE such that we can roughly correct for the foreground contamination. This issue is evident at the stage of combining the spectra from the three different nights: two of the masks of the MODS masks (#505919 and #510122) were aligned at a PA of −14 deg, nearly orthogonal to the orientation between the foreground object and the LAE in the WFC3 images (see Fig. 4). The third mask (#523405) was aligned at PA = 50 deg, closer to parallel between the orientation of the two components. A greater degree of foreground contamination would be expected in this mask, and indeed, the EW of Ly α measured from this spectrum – using a direct fit to the observed continuum – is nearly half

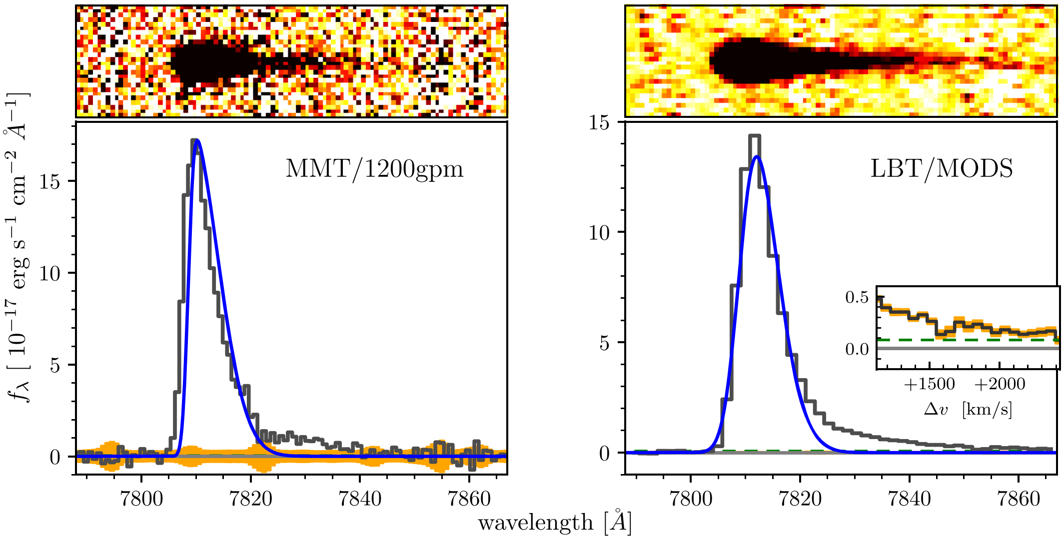

Figure 7. Ly α emission profiles from the MMT/Red Channel 1200 gpm spectrum (left) and LBT/MODS (right). The upper panels display the 2D spectra over an extent of 8 arcsec for the MMT spectrum and 6 arcsec for the LBT spectrum (the LBT spectrum has been binned by a factor of 2 along the spatial axis for display purposes). In the lower panels, the orange-shaded regions span the $\pm 1\sigma$ errors, and the green dashed lines mark the continuum level obtained from fitting the spectrum at $\sim$8000 Å. The blue line shows the result of the truncated Gaussian profile fit, convolved with the profile of each instrument. This profile fits the core of the line reasonably well but fails to account for the extended red wing of the line. The inset panel displays a zoom on the MODS spectrum, showing that the flux drops only to the continuum level at $\sim$7870 Å, corresponding to +2300 km s^{-1} from the peak of the Ly α emission. We compared the 2D profile of the high *S/N* MODS spectrum with reference stars included in the same slit mask and see no evidence for spatially extended Ly α emission at $\sim$1 arcsec resolution.

Table 3. Photometry obtained from multiband fitting to *HST* images, with the exception of FR782N, which is obtained from aperture photometry using `SExtractor` MAG_AUTO.

Component	$(\Delta(\alpha), \Delta(\delta))$	F606W	FR782N	F850LP	F125W	F160W
			Two-component model			
PSF(A)	(+0.000, +0.000)	27.10 $\pm$ 0.18	20.79 $\pm$ 0.04	23.64 $\pm$ 0.02	23.84 $\pm$ 0.01	23.95 $\pm$ 0.01
Sers(B+C)	($-$0.103, $-$0.260)	25.30 $\pm$ 0.10	>24.6	24.43 $\pm$ 0.17	23.94 $\pm$ 0.02	23.70 $\pm$ 0.02
			Three-component model			
Sers(A)	(+0.000,+0.000)	27.27 $\pm$ 0.89	20.79 $\pm$ 0.04	23.54 $\pm$ 0.02	23.71 $\pm$ 0.01	23.80 $\pm$ 0.01
Sers(B)	($-$0.142, $-$0.307)	26.47 $\pm$ 0.53	>24.6	25.27 $\pm$ 0.78	24.43 $\pm$ 0.23	24.37 $\pm$ 0.40
Sers(C)	(+0.017, $-$0.313)	25.87 $\pm$ 0.42	>24.6	27.27 $\pm$ 5.55	25.92 $\pm$ 0.27	25.14 $\pm$ 0.21

that measured from the other two spectra. We note that there is no evidence for spatially extended emission in the 2D spectra at the resolution of the LBT seeing ($\sim$0.6–1.0 arcsec).

The full LBT/MODS1 spectrum is presented in Fig. 3, while a zoom on the Ly α feature in both the LBT and MMT/1200 gpm spectra can be seen in Fig. 7. Results obtained from analysis of the spectra are given in Table 4.

$_{\text{Ly}\,\alpha}$*Ly α emission:* We first examine the strong Ly α emission feature. We extract a line flux by integrating the spectrum between 7800 Å and 7850 Å after subtracting a fit to the continuum redward of the line at 8000 Å. This observed flux – 11.5 $\times$ 10^{-16} erg s^{-1} cm^{-2} – is exceptionally large, even when compared to other lensed galaxies at high redshift. Ignoring gravitational lensing,[4] this corresponds to a line luminosity of $L \sim 4 \times 10^{44}$ erg s^{-1}. We obtain a raw EW$_0$(Ly α) = 214 $\pm$ 5 Å using the continuum fit. We estimate the contaminating flux of the foreground object to the continuum using the *HST* photometry; after removing this flux, we obtain a corrected value of EW$_0$(Ly α) $\sim$260Å, in excellent agreement with the results from the *HST* narrowband image (Section 3.3). We also derive a simple non-parametric estimate for the linewidth by measuring the red Half-Width at Half-Maximum (rHWHM; the width of the red side of the line profile at half of the peak value). Using the higher resolution MMT/1200-gpm spectrum and correcting for the instrumental profile (FWHM $\sim$100 km s^{-1}), the measured rHWHM is 160 km s^{-1}.

It can be seen from Fig. 7 that the Ly α emission extends to >2000 km s^{-1} redward of the peak. This can be compared to a z = 5.7 LAE reported by Yang et al. (2014) to have a red wing extending >1000 km s^{-1} from the peak of the Ly α emission and similar ‘shoulders’ observed in the red wings of bright, high-redshift LAEs (e.g. Lidman et al. 2012; Smit et al. 2017). As with these examples, J1414+5446 is sufficiently bright – both in the continuum and line emission – to permit detailed studies of the line profile.

The observed features of the Ly α spectrum can be attributed to scattering through an outflow, which is usually represented as an expanding, dusty shell of neutral hydrogen (Verhamme et al. 2008; Gronke et al. 2015). We apply the automated fitting routine described in Gronke et al. (2015) to find the best-fitting shell model for the observed Ly α profile. Briefly, this method fits a model with six shell model parameters to the observed spectrum: expansion

[4]The lensing correction is highly uncertain and will be discussed in Section 4.5.

Table 4. Summary of physical quantities obtained from analysis of the LBT spectrum and *HST* imaging.

Property	Value
R.A. (J2000)	14:14:46.827
Decl. (J2000)	+54:46:31.94
z(Ly α)	5.4253 (from peak wavelength)
rHWHM(Ly α)	160 km s^{-1} (from MMT/1200 gpm)
flux(Ly α)	$(11.5 \pm 0.3) \times 10^{-16}$ erg s^{-1} cm^{-2}
EW$_0$(Ly α)	214 ± 5 Å($\sim$260 Å from phot.)
$L_{\mathrm{Ly}\,\alpha}$[a]	$(3.8 \pm 0.1) \times 10^{44}$ erg s^{-1}
SFR(Ly α)[a]	390 ± 10M$_{\odot}$ yr^{-1}
z(N IV] 1486)	5.4237
FWHM(N IV] 1486)	344 ± 26 km s^{-1}
flux(N IV] 1486)	$(3.8 \pm 0.3) \times 10^{-17}$erg s^{-1} cm^{-2}
EW$_0$(N IV] 1486)	7 ± 3 Å(11 Å from phot.)
Δv(Ly α-NIV])	$+72 \pm 13$ km s^{-1}
EW$_0$(N V)	<0.24 Å(<0.5 Å from phot.)
EW$_0$(C IV)	$\lesssim$ 17 Å($\lesssim$27 Å from phot.)
M_{1350}[a]	−22.99 (from phot.)

Notes. Rest frame EWs are given in units of Å, line fluxes in erg s^{-1} cm^{-2}, continuum flux densities in erg s^{-1} cm^{-2} Å^{-1}, luminosities in erg s^{-1}, and SFRs in M$_{\odot}$ yr^{-1}. The reported position is from the *HST* F850LP image. The redshift estimate is obtained from the pixel wavelength corresponding to the peak flux density. Values indicated as being derived from photometry are obtained from the continuum fit to the resolved *HST* photometry. EW errors include a factor of 50 per cent uncertainty on the continuum level.
[a] No lensing correction has been applied to the luminosities or quantities derived from them.

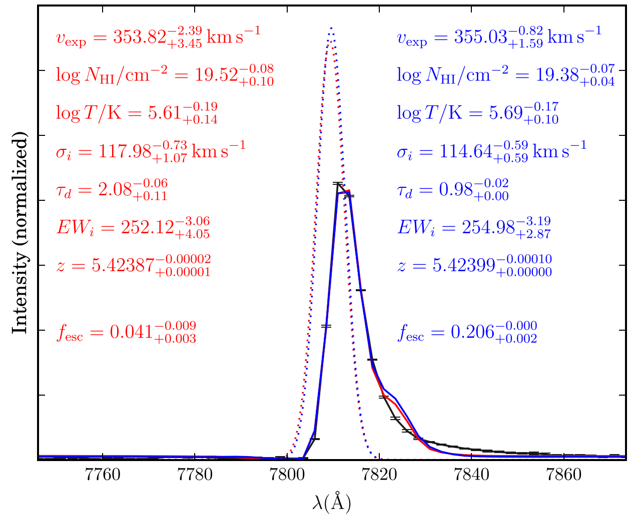

Figure 8. Results of shell model fits to the Ly α line using the automated procedure from Gronke et al. (2015). The black line shows the observed spectrum, with horizontal error bars overlaid. The dashed lines show the intrinsic Ly α profiles from the model fits; the model with a large τ_{d} is shown in red and the model with a strong dust prior is shown in blue. The solid lines show the resulting profile after including radiative transfer through the expanding shell. Parameter values for the fit with large τ_{d} are given on the left and for the constrained τ_{d} on the right.

velocity (v_{exp}), hydrogen column density (N_{HI}), effective temperature (T), intrinsic dispersion of the Ly α line (σ_{i}), dust optical depth (τ_{d}), and the intrinsic equivalent width of the line (EW$_{\mathrm{i}}$). In addition, the systemic redshift (z) is included in the fit. The best fit is determined through a χ^2 minimization and the likelihood surfaces are characterized with a Markov Chain Monte Carlo (MCMC) approach. Further details of the fitting technique, including the parameter space explored by the simulations, may be found in Gronke et al. (2015).

$_{\mathrm{Ly}\,\alpha\,\mathrm{Ly}\,\alpha}$Fig. 8 presents the results of the shell model fits. The *solid red line* represents the best-fitting model obtained after imposing a narrow Gaussian prior with $\sigma_v = 15$ km s^{-1} and centred at $z = 5.4237$. These values were selected based on the results of fitting the N IV] line, which we assume to be at the systemic redshift. The data require (v_{exp}, $\log N_{\mathrm{HI}}$) $\sim$ (350 km s^{-1}, 19.5). The observed Ly α line shift of $\Delta v \sim$70 km s^{-1} primarily sets the constraint on v_{exp}. The intrinsic width of the Ly α line is found to be FWHM$_{\mathrm{int}}$ $\sim$ 250 km s^{-1}. The latter is in remarkably good agreement with the width inferred from the N IV line (see below). What is surprising is that the best-fitting model favours the shell to be dusty, with $\tau_{\mathrm{d}} \sim$2. This translates to Ly α escape fractions of $f_{\mathrm{esc}} \sim$10 per cent. Given the large EW of the Ly α emission from this galaxy, this low Ly α escape fraction is not likely to be physical. The *solid blue line* shows the best-fitting model, if we force a lower τ_{d} through a strong prior and also fix the redshift at $z = 5.24$. The data still favour dusty solutions with $\tau_{\mathrm{d}} \sim$1.0 (the other model parameters are barely affected), leading to an Ly α escape fraction of $f_{\mathrm{esc}} \sim$30 per cent. This is still low but at least consistent with inferred Ly α escape fractions for galaxies that have similar Δv (e.g. Erb et al. 2014; Yang et al. 2017). It is not possible to find shell model solutions with lower τ_{d}: the observed velocity shift of the Ly α line constrains the parameters (v_{exp}, $\log N_{\mathrm{HI}}$). Generally, Ly α scattering broadens spectral lines in the absence of dust. In the presence of dust, scattering and spectral broadening are limited. The observed narrowness of the Ly α spectral line (and the absence of a blue peak) then requires at least some dust. Another possibility to be considered at this high redshift is the impact of the IGM that also narrows the observed Ly α line and extinguishes the blue peak (Dijkstra, Lidz & Wyithe 2007), thus, mimicking the effect of dust (as discussed in Gronke 2017).

The simple shell model has difficulty reproducing both the observed shift of the line ($\Delta v \sim$70 km s^{-1}) and the very extended red wing. With a narrow prior on redshift, the model fails to reproduce the observations at $\lambda > 7825$ Å (corresponding to $\Delta v > 500$ km s^{-1}). If a wide redshift prior is employed, the model is able to reproduce the extended red wing but underpredicts the overall shift of the line. This likely represents a shortcoming of the shell model. This tension could be alleviated by introducing a velocity gradient in the shell that would tend to 'smear out' the observed spectrum (e.g. Loeb & Rybicki 1999).

N V emission: There is no N V λ1240 emission as would be expected from an Active Galactic Nucleus (AGN). The continuum is detected at $\sim$4 σpix^{-1} in the region where N V would be located (and has relatively little foreground contamination); combined with the extremely large flux of the Ly α line, we obtain a stringent constraint of f(N V)/f(Ly α) <10^{-3}(1σ), compared to $\sim$10 per cent for narrow-line AGN (Alexandroff et al. 2013).

N IV] emission: The only other clear detection of an emission line in the LBT spectrum is at 9549 Å. We identify this line as NIV] 1486.5. While this emission line is rarely observed, it has been found in a galaxy with very similar properties to the one presented here. GDS J033218.92-275302.7 at $z = 5.56$ has EW(N IV] 1486.5) $\approx$30 Å (Vanzella et al. 2010). This emission feature is a doublet, but in both cases no emission corresponding to N IV] 1483.3 is detected (we obtain a limit of f(N IV] 1483) $<1 \times 10^{-17}$ erg s^{-1} cm^{-2}). The width of the line is FWHM = 260 ± 40 km s^{-1} after correcting for instrumental resolution. The N IV] emission feature is displayed in Fig. 9.

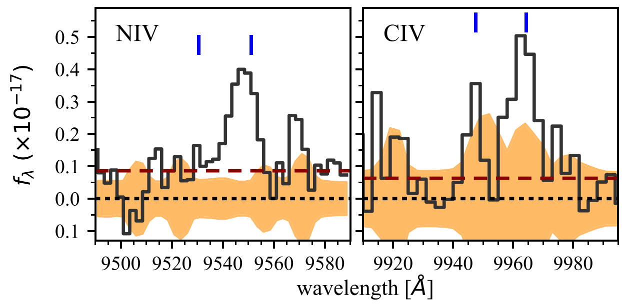

Figure 9. Zoom on the LBT spectrum at the wavelengths of the N IV] and C IV emission lines. The spectral flux density is represented by the solid lines and the $\pm1\sigma$ noise level by the orange-shaded region. The continuum level is denoted with a red dashed line. The blue vertical lines mark the expected locations of the doublet features for both lines using the redshift obtained from the peak of the Ly α line.

C IV emission: The expected wavelength of C IV λ1550 is at 9950 Å. Unfortunately, this is in a spectral region with strong night sky emission lines. The spectrum obtained from `modsidl` processing appears to have significant positive flux in this region (see Fig. 3), but the sky subtraction in this region did not seem to be reliable. We reprocessed the 2D spectra in this region using a custom 2D spline fit to the background sky emission. The sky subtraction residuals improved considerably after this reprocessing and the residual flux decreased; however, a small positive flux remains. Fig. 9 displays the reprocessed spectrum. Although the positive flux residual lies almost exactly at the wavelengths expected for the C IV doublet, these wavelengths also align closely with two particularly strong night sky lines and it is difficult to assign a significance to the flux. Taking the noise model for the sky background at face value, we obtain a flux of *f*(C IV) $\lesssim 6\times10^{-17}$erg s^{-1} cm^{-2}. This flux is well below expectation for an AGN, with a flux ratio *f*(C IV)/*f*(Ly α) $\lesssim$ 0.06, compared to $\sim$0.2–0.5 for narrow-line AGN (Alexandroff et al. 2013; Ferland & Osterbrock 1986).

ISM absorption features: Given the bright continuum flux of J1414+5446, we are able to obtain constraints of faint interstellar medium (ISM) absorption and emission features. These features provide important diagnostics of the kinematics and covering fraction of neutral gas in the ISM. Stacking analyses provide the best constraints on the strengths of these features in typical $z > 3$ LBGs (e.g. Jones et al. 2012); however, a few such galaxies are sufficiently bright for individual study (e.g. Christensen et al. 2012; Bayliss et al. 2014; Patrício et al. 2016). In our case, the deep LBT spectrum of a $z = 5.4$ galaxy achieves only *S/N* $\sim$3pix^{-1} at $\gtrsim$1200 Å, and the foreground contamination further reduces the sensitivity to faint spectral features. Nonetheless, we examine several of the ISM features previously studied by Jones et al. (2012) in stacked 3 $< z <$ 7 LBGs, using the wavelengths and velocity offsets listed in their Table 1, and adopting Gaussian profiles with widths tuned to match their composite spectrum.

No ISM features are clearly detected in the LBT spectrum. Si II λ1260 has a marginal detection, with $W = -0.5 \pm 0.4(1\sigma)$. The Si II* λ1264 fine structure line is also marginally detected, with $W = 0.3 \pm 0.2$, as well as Si II* λ1309, with $W = 0.5 \pm 0.3$. We obtain limits of $W < 0.4$ Å on the OI+Si II λ1303 feature, and $W < 0.2$ Å on CII λ1334. All other features are too strongly affected by night sky lines to produce meaningful constraints. We have not attempted to correct for the foreground contamination in these measurements; they mainly serve as a guide as to what level of constraint we can obtain given the quality of the available spectrum.

In general, the lack of strong ISM absorption features is consistent with the trend that the equivalent widths of such features anti-correlate with the strength of the Ly α emission, as detailed in Jones et al. (2012). Thus, we would not have expected to see ISM features in the spectrum of J1414+5446. However, given the strength of the observed continuum flux, an even deeper spectrum obtained with a 30m class telescope would place stronger constraints on the physical conditions of the ISM in this galaxy.

4.3 Ionizing spectrum

We argued in the previous subsection that J1414+5446 lacks the spectroscopic signatures of AGN. However, the N IV] detection and questionable C IV detection indicate that the nebular gas is subjected to a hard radiation field that is able to ionize these higher order species, with ionization potentials of 47.4 eV and 47.9 eV, respectively. Nebular CIV detections have been reported in lensed galaxies at $z = 7.045$ (Stark et al. 2015b), $z = 6.11$ (Mainali et al. 2017), and $z = 4.88$ (Smit et al. 2017). N IV] has been found in a massive galaxy at $z = 5.56$ (Vanzella et al. 2010) and in lensed galaxies at $z = 3.4$–3.5 (Fosbury et al. 2003; Patrício et al. 2016). While in none of these galaxies – including the one reported here – can an AGN contribution be definitively ruled out, photoionization modelling shows that a population of very hot, massive stars could account for the observed nebular emission, in particular, the detections of high-ionization species such as NIV]/C IV without N V emission as expected from an AGN (e.g. Fosbury et al. 2003). These conditions may be more prevalent during the early stages of galaxy formation, and bright sources like J1414+5446 demonstrate the promise of rest-UV spectroscopy for probing the physical conditions of distant galaxies. It is also noteworthy that NIV] is not detected in many galaxies with C III and C IV emission (e.g. Stark et al. 2014), indicating that it may arise only in particular conditions requiring more than just a hard radiation field.

4.4 Ly α velocity offset

The detection of UV metal lines further provides a measure of the systemic redshift of the galaxy (e.g. Stark et al. 2015a). The velocity offset of the Ly α line ($\Delta v_{\mathrm{Ly}\,\alpha}$) is sensitive to the covering fraction and kinematics of neutral hydrogen; as discussed in Section 4.2, the Ly α profile of J1414+5446 is broadly consistent with an expanding, dusty shell of neutral gas. Here, we examine the velocity offset of Ly α relative to the NIV] emission line. The offset between the centroid of the N IV] line and the peak of the Ly α is 70 km s^{-1}. Stark et al. (2015a) measured $\Delta v_{\mathrm{Ly}\,\alpha}$ for two lensed $z \sim 6$ galaxies with systemic redshifts from C III] nebular emission and found smaller offsets than galaxies at $2 < z < 3$; however, Willott et al. (2015) detected relatively large (>400 km s^{-1}) offsets in two luminous $z \sim 6$ galaxies with systemic redshifts from [C II]λ158 μm and argued that the observed offsets are consistent with the overall trend between $\Delta v_{\mathrm{Ly}\,\alpha}$ and EW$_{\mathrm{Ly}\,\alpha}$ seen at lower redshift. The relatively small velocity offset found for J1414+5446 by adopting the N IV] redshift is similar to the results of Smit et al. (2017), who found an offset <100 km s^{-1} for a lensed $z = 4.88$ galaxy with an extended Ly α halo (and similarly large Ly α EW). Larger velocity offsets aid the escape of Ly α photons through the high-redshift IGM (e.g. Stark et al. 2016), and thus galaxies with both small velocity offsets and large Ly α equivalent widths are highly intriguing.

4.5 Lensing model

The lensing group SL2S J141447+544703 was identified by the SL2S (Cabanac et al. 2007) based on the detection of a tangential arc (T1) and a candidate bright radial arc (R1). More et al. (2012) subsequently identified an additional radial arc candidate (R2), bringing the total number of lensed galaxy candidates associated with SL2S J141447+544703 to 3. Images of the three candidate arcs can be viewed in Fig. A2 in Appendix A.

Cabanac et al. (2007) estimated a photometric redshift of $z = 0.75$ for the galaxy group, while More et al. (2012) estimated $z_{\rm lens} = 0.63 \pm 0.02$. We included several candidate group member galaxies in our MODS mask; more complete details are provided in Appendix A. We obtain a mean redshift of $\langle z_{\rm lens}\rangle = 0.613$ from spectra of 43 galaxies in the group, in excellent agreement with the More et al. (2012) photometric redshift.

The lensing properties of SL2S J141447+544703 have been discussed in a number of publications. More et al. (2012) quote an arc radius of 14.7 arcsec for the tangential arc T1. Foëx et al. (2013) report a photometric redshift of $z_s = 1.47^{+0.75}_{-0.53}$ for the arc and used a shear profile analysis to obtain a velocity dispersion of $\sigma_{\rm SIS} = 969^{+100}_{-130}\,{\rm km\,s^{-1}}$ for the lens, roughly at the boundary between a group- and cluster-scale lensing mass. Recently, Gruen et al. (2014) identified SL2S J141447+544703 with a galaxy cluster detected by the Planck satellite through the Sunyaev-Zel'dovich (SZ) effect (Planck Collaboration et al. 2014b). Gruen et al. (2014) update the results of Foëx et al. (2013) and obtain a significantly larger velocity dispersion through weak lensing analysis, $\sigma_{\rm SIS} = 1540^{+162}_{-190}\,{\rm km\,s^{-1}}$. Their measurement of the halo mass is $M_{500c} \approx 20 \times 10^{14} h_{70}^{-1}{\rm M}_{\odot}$ from weak lensing and $M_{500c} \approx 8 \times 10^{14} h_{70}^{-1}{\rm M}_{\odot}$ from the SZ detection. These larger estimates favour a cluster scale for the foreground mass.

Gruen et al. (2014) note that a redshift of $z_s = 1.49$ for the source galaxy of the tangential arc is favoured by their mass model in order to match the observed arc radius, in agreement with the photometric redshift estimate from Foëx et al. (2013). Spectroscopic redshifts for the candidate arcs are strongly constraining on the lens mass models and hence we observed all three arcs with MODS. For R1 and R2, we obtain redshifts that place them in the foreground of the cluster. For T1, we do not detect any emission lines in the MODS spectra; however, the strongest available line would be [O II] $\lambda3727$, which at $z \gtrsim 1.5$ would be at wavelengths dominated by OH sky lines and thus difficult to detect. Further details of the MODS spectroscopy of targets in the field of J1414+5446 are given in Appendix A.

We first consider a rough estimate for the lensing magnification of the LAE based on a few simplifying assumptions. J1414+5446 is $\sim$30 arcsec from the apparent cluster centre based on the brightest cluster galaxy position and is thus at a radius of $\approx 2\theta_{\rm E}$, where $\theta_{\rm E}$ is the Einstein radius. As an example, if we assume an arc redshift of $z \approx 2$, the lensing magnification from the cluster alone would be $\mu \approx 3$. However, additional magnification from the foreground galaxy must also be taken into account. Adopting the Faber–Jackson relation given in Bernardi et al. (2003) and assuming the foreground galaxy is at the cluster redshift ($z = 0.6$) yield a velocity dispersion $\sigma_v \approx 85$ km s^{-1} and $\theta_{\rm E} = 0.2$ arcsec. Although the Faber–Jackson relation may not be appropriate for this galaxy, this rough estimate demonstrates that the LAE may lie near the Einstein ring radius. Thus, the magnification is difficult to constrain and may be rather large. The *HST* narrowband imaging provides strong evidence against multiple-image strong lensing of the Ly α-emitting component. The WFPC2 imaging of the far-UV continuum is more ambiguous in that the multiple components are suggestive of a strong lensing configuration. However, we argued in Section 3.2 that only a single component in the WFPC2 image is likely associated with the LAE based on the observed colours. Thus, while some ambiguity remains (which could be resolved with further *HST* or JWST observations), the available *HST* imaging disfavours multiple-image strong lensing.

In order to better constrain the lensing magnification, we model the cluster mass through an MCMC approach using the LENSTOOL software (Jullo et al. 2007), which fits the normalization of the Faber–Jackson scaling relation. The input data are the cluster member galaxies with redshifts from MODS spectroscopy and photometry from *HST*. The model includes the contribution from the foreground galaxy, which can produce a wide range of amplifications depending on the assumed mass. We thus fold in the photometric uncertainties on the foreground galaxy and make the simplifying assumption that it lies at the cluster redshift.

We execute a series of Monte Carlo simulations that convolve the uncertainties on both the normalization of the scaling relation and the foreground galaxy mass, excluding models that result in multiple image lensing of the LAE (treated as a geometric point source) as the *HST* imaging suggests that this is unlikely. Finally, we assume a redshift for the lensed arc. The total amplification increases with decreasing arc redshift; in fact, $z = 1.5$ is essentially ruled out as this invariably results in multiple images. In the *HST* imaging, it is apparent that the lower part of the arc T1 is coincident with an unassociated source of roughly equal brightness. The two objects are blended in the CFHT imaging and this may have affected the previously reported photometric redshifts for the arc (i.e. biasing them to lower redshift). We also note that the large mass estimates from Gruen et al. (2014) would produce multiple images of the LAE at other locations in the cluster field, which we do not identify in the *HST* or CFHT images.

Compared to previous mass modelling of this system, our approach has the advantage of self-consistently including the new member galaxy redshifts we have obtained, the new constraints on the lensed arc candidate redshifts, and most crucially, the presence of the foreground galaxy near the LAE position that strongly perturbs the local magnification map. This results in a highly non-linear estimate for the total lensing magnification of the LAE. Furthermore, the unknown redshift for the lensed arc T1 adds considerable uncertainty to our magnification estimate. We thus investigate the impact of the arc T1 redshift on the LAE magnification by considering three discrete values of redshift in the range $1.5 < z \le 2.5$[5] in order to explore the uncertainty of the magnification factor.

Fig. 10 presents the distribution of lensing amplifications obtained from these simulations. For $z = 2$, the median and interquartile ranges are $\mu = 17^{+4}_{-3}$. At $z = 2.5$, this drops to $\mu = 8^{+1.4}_{-1.0}$. Given all the uncertainties involved in this analysis, we adopt $5 \lesssim \mu \lesssim 25$ as a conservative estimate for the range of allowed magnifications, thus the intrinsic luminosity of J1414+5446 is poorly constrained. It is likely that the source is intrinsically round and experiencing a relatively low magnification, although scenarios in which the intrinsic source shape conspires with the lensing geometry to produce a high magnification event with little apparent stretching cannot be ruled out. A spectroscopic redshift for the lensed arc T1 would reduce the uncertainty on the magnification but still allow a wide range of values. JWST will have the capability to obtain resolved near-IR spectroscopy of both the foreground interloper and the LAE and

[5] The arc is unlikely to lie at $z > 2.5$, given that it is detected in the u-band.

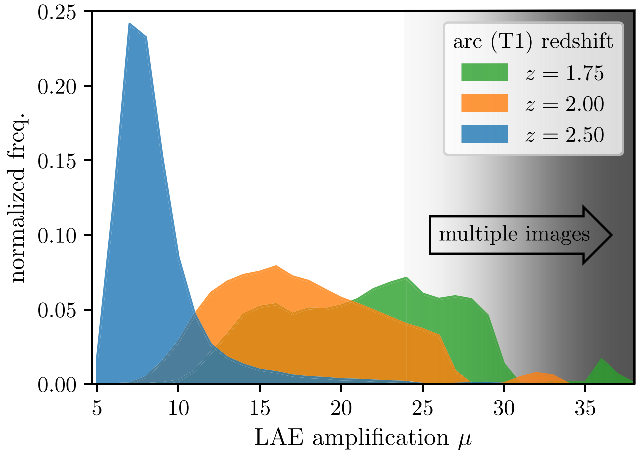

Figure 10. Lensing amplification factors for J1414+5446 under three assumptions for the redshift of the lensed arc T1. The histograms are the result of Monte Carlo simulations accounting for uncertainties in the foreground interloper photometry and hence its estimated mass, assuming that it lies at the redshift of the cluster. Simulations with $\mu \gtrsim 25$ tend to result in multiple images and are unlikely, given the observational constraints.

Table 5. Photometry for the foreground galaxy from CFHT and *HST*.

Band	AB mag
u	26.45 ± 0.28
g	26.58 ± 0.23
V_{606}	25.30 ± 0.10
z_{850}	24.43 ± 0.17
H_{160}	23.70 ± 0.02

thus provide robust constraints on the lensing amplification of this high-redshift galaxy.

4.6 Broadband SED

We further characterize the properties of J1414+5446 through a detailed analysis of its SED. Before attempting to fit the SED, we must first deblend the foreground contribution from the observed fluxes, particularly in the long wavelength bands where the emission is completely unresolved. We approach this problem by constructing SED templates for the foreground galaxy that reproduce the (semi-)resolved photometry in the bluer bands and use these templates to account for the foreground contribution to the redder bands. This compares to Section 3.2, where we took advantage of the higher resolution provided by *HST* to obtain deblended photometry of the foreground and LAE at $\lambda < 2\,\mu$m (we consider this photometry to be 'semi'-resolved in that the peaks of the two primary objects are well separated, but the light profiles are significantly blended). Here, we attempt to use simple assumptions about the SED of the foreground galaxy to obtain constraints on the long-wavelength fluxes of the LAE.

The u- and g-band detections are absent and any contribution from the LAE and those fluxes can be assigned to the foreground. The *HST* data provide photometry from 0.6–1.6 μm, where we adopt the two-component model from Table 3 and attribute the fluxes from B+C to the foreground. The resulting photometry is provided in Table 5. Panel (a) in Fig.11 displays the resulting SED for the foreground galaxy, where the points at $\lambda < 2\,\mu$m represent the (semi-)resolved photometry.

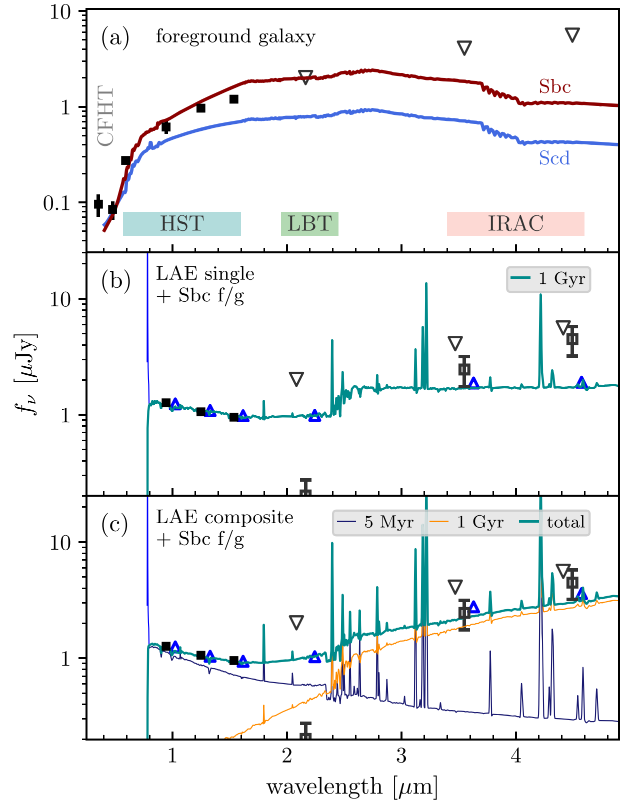

Figure 11. Photometry and results from SED fitting. The black points with error bars represent the resolved CFHT and *HST* photometry. The inverted triangles mark the blended photometry from the LBT and Spitzer. Panel (a) shows SED models assumed for the foreground galaxy. Based on the optical photometry, the foreground SED is likely to lie between the Sbc and Scd templates; this provides a range of values used for subtracting the foreground contamination to the infrared data. Panels (b) and (c) present fits to the SED of the $z = 5.4$ LAE. The grey points with error bars are obtained subtracting the foreground contamination assuming an Sbc SED. The fits are performed to these 'decontaminated' data. Panel (b) displays the fit for a single-stellar population model with a continuous star formation history, while panel (c) presents a composite model consisting of a young (5 Myr) starbursting component and an evolved (1 Gyr) population. The blue triangles mark the photometry recovered from the SED fits, offset slightly in wavelength.

In order to infer the contribution of the foreground to the total fluxes at $\lambda > 2\,\mu$m, we employ the template SEDs from Coleman, Wu & Weedman (1980). These empirical templates are adopted as they provide a small number of simple galaxy archetypes that we utilize to roughly span the range of possible SEDs for the foreground galaxy. We make the simplifying assumption that the foreground galaxy lies at the redshift of the SL2S J141447+544703 group.[6] After fitting to the $\lambda < 2$-μm data, we find that an Sbc template represents the 'maximal' contribution from the foreground galaxy that provides a reasonable fit to the resolved *HST* photometry. A bluer Scd template is a better match to the $u - g$ colour from the CFHT photometry but a poorer match to the *HST* data. Panel (a) of Fig. 11 compares these templates to the observed SED of the foreground galaxy. The contributions to the total fluxes (Table 1) in the longer wavelength bands for the Sbc (Scd) template are ∼90

[6]The foreground galaxy is likely to be at low redshift, given the marginal u-band detection.

per cent (40 per cent), 40 per cent (20 per cent), and 20 per cent (10 per cent) for the K_s-, 3.6-μm, and 4.5-μm bands, respectively.[7]

Having characterized the SED of the foreground galaxy, we construct the SED for the $z = 5.4$ LAE from the *HST* photometry, the LUCI K_s-band image, and the Spitzer/IRAC data. In total, we have six data points spanning 1400–7000 Å in the rest frame of J1414+5446. We construct two versions of the SED, alternately using the Sbc or Scd template fits to subtract the foreground contamination to the K_s/3.6/4.5 bands. We further inflate the photometric errors in these bands by 0.3 mag in order to account for the uncertainty associated with the foreground removal. The Sbc foreground template is more conservative in the sense that it results in smaller fluxes for the LAE in the IRAC bands; the SED obtained after subtracting the Sbc foreground template is displayed in panels (b) and (c) of Fig. 11.

The deblended SED for the LAE is then fit with the method described in Stark et al. (2013), which includes models for nebular emission presented in Robertson et al. (2010). Briefly, the stellar population is represented with templates from the (Bruzual & Charlot 2003) models, and the nebular emission is self-consistently included by using the ionizing photon output from the stellar population. Accounting for the nebular emission in this galaxy is important as H α lies in the 4.6-μm band and [O III] lies in the 3.6-μm band (H β is just outside of this band). In all fits, we exclude the K_s band, as it has the largest degree of uncertainty in terms of the foreground contribution. The best-fitting stellar template is found using a grid search of the stellar population parameters and identifying the template with the minimum χ^2 calculated from the observed photometry. Dust extinction is included using the Calzetti, Kinney & Storchi-Bergmann (1994) relation.

The result of the single population fit is shown in Fig. 11(a). We find that a single-stellar population model provides a poor fit to the observed SED. The best-fitting model has an age of 1 Gyr, a star formation rate (SFR) of $\sim$50 M$_\odot$ yr^{-1} (assuming a constant star formation history), and a stellar mass of 3.5×10^{10} M$_\odot$, and no dust. The statistical errors on these quantities are at the $\sim$10–30 per cent level; however, the uncertainties are dominated by systematics in the foreground removal and lens magnification estimate. The results are similar whether the Sbc or Scd template is adopted for the foreground.

We next consider a two-component model. This additional flexibility allows for a young population to account for the blue UV SED, while an older population – implying significant past star formation – accounts for the bright IRAC fluxes. Given the small number of photometric data points and the systematic uncertainties mentioned above, the results from these fits must be approached with caution. Nonetheless, we find that the best-fitting model includes a young (starburst) component with a fixed age of 5 Myr, an (constant) SFR of $\sim$100 M$_\odot$ yr^{-1}, and a stellar mass of $\sim 6 \times 10^8$M$_\odot$. The evolved component has an age of 1 Gyr, SFR $\sim$400 M$_\odot$ yr^{-1}, and stellar mass $\sim 3 \times 10^{11}$M$_\odot$, again assuming a constant star formation history. The evolved population also has $E(B-V) = 0.44$. These values change by only $\sim$10 per cent whether the Sbc or Scd foreground model is used. As can be seen in Fig. 11(b), the composite model performs much better at reproducing both the blue UV slope and the bright IRAC fluxes. For the Sbc template, the single population model has a total $\chi^2 = 8.2$ for five data points, while the composite model has $\chi^2 = 2.9$. In both cases, the number of model parameters is large compared to the number of data points and thus the χ^2 statistic should be approached with caution, but this does indicate a significant improvement with the composite model.

In performing these SED fits on the observed fluxes, we are ignoring any magnification due to gravitational lensing. As an example, an arc redshift of $z = 2.5$ would reduce the inferred stellar masses and ages by a factor of $\sim$8, suggesting that J1414+5446 is a moderately massive galaxy with a substantial population of older stars. However, an arc redshift of $z \lesssim 2$ would suggest that the true stellar mass is lower by more than an order of magnitude. In our fits, we have constrained the stellar age to be less than the age of the universe at $z = 5.4$, but the observed fluxes push the ages close to this limit. This tension is significantly reduced after correcting for a factor >5 lens magnification that would significantly decrease the inferred age. Regardless of the total stellar mass, the strong emission lines and blue UV slope point toward an ongoing starburst. J1414+5446 will be a prime target for JWST, which can provide resolved photometry and spectroscopy at rest frame optical wavelengths – including the Balmer series emission lines – and greatly improved constraints on the current and past star formation in this unusual galaxy.

4.7 Star formation

There are multiple indicators available to estimate the SFR in J1414+5446. The UV continuum traces the (relatively) unobscured star formation. Adopting the continuum fit from the *HST* imaging ($M_{1350} = -23.0$, $\beta_\lambda = -2.6$) and applying the relation from Madau, Pozzetti & Dickinson (1998) for a Salpeter IMF and ignoring dust extinction, we obtain a value of $\approx$80 M$_\odot$ yr^{-1}. This is consistent with results for the younger stellar population in the two-component SED fits presented in Section 4.6, which are $\sim$100 M$_\odot$ yr^{-1}. On the other hand, the evolved population from the SED fits has a substantial component of dust-obscured star formation, with SFR $\approx$ 400 M$_\odot$ yr^{-1} and $E(B-V) \approx 0.4$. The luminosity of the Ly α line is also consistent with a large SFR. Ignoring dust extinction and applying the Kennicutt (1998) calibration for H α (assuming Case B recombination and ignoring lensing) to the line luminosity obtained from spectral fitting yields SFR(Ly α) $\gtrsim$ 400 M$_\odot$ yr^{-1}. The line luminosities from both the narrowband imaging and the model fitting are $\sim$20 per cent larger; note the latter implicitly includes a dust correction. From both the SED and Ly α profile fitting, we conclude that a substantial amount of obscuring dust may be present, implying a much larger Ly α SFR after dust correction, which we do not perform here. The gravitational lensing correction acts in the opposite direction and would bring the estimates down by anywhere from a factor of 5–25. We conclude that the intrinsic SFR is roughly consistent with being in the range of $\sim$10–100 M$_\odot$ yr^{-1}.

5 CONCLUSIONS

We present extensive observations of an unusual high-redshift-lensed galaxy. CFHTLS J141446.82+544631.9 was initially targeted as a quasar candidate within the CFHTLS but proved to be an exceptionally bright galaxy at $z = 5.426$. Our observations lead to the following picture of this interesting object:

(i) The galaxy is unusually bright for a (likely) non-AGN at $z = 5.4$ and has one of the largest Ly α fluxes reported to date. The

[7] We also examined photometry of field galaxies covered by the same imaging bands and found that those with SED shapes most similar to the foreground galaxy fell between the Sbc and Scd templates, bolstering the case for using these to bracket the possible foreground contamination.

UV continuum is easily detected and has SNR∼3 in a moderate-resolution LBT/MODS1 optical spectrum.

(ii) The strong Ly α emission from this galaxy suggests a powerful starburst and sightlines through which Ly α photons can escape. The broad red wing of the line extends over ∼2000 km s^{-1} as expected from an outflowing shell. The peak of the Ly α emission is redshifted by ∼70 km s^{-1}.

(iii) Typical AGN emission lines such as N V and C IV are not detected. However, the N IV] line is detected. Only a few examples of strong N IV] emitters exist in the literature; this may be associated with a large population of massive stars keeping the nebular gas in a hot, highly ionized state.

(iv) Fits to the observed SED prefer a two-component model, with a young population to fit the blue UV slope found with resolved *HST* photometry, and a massive, evolved population indicated by bright IRAC fluxes.

(v) J1414+5446 lies behind a massive lensing group and has a spatially proximate, faint galaxy in the foreground. This leads to a highly uncertain estimate for the total magnification from gravitational lensing, with values in the range $5 \lesssim \mu \lesssim 25$.

(vi) The unobscured SFR inferred from the Ly α flux, UV continuum, and UV/optical SED of this galaxy all suggest that it is forming stars at a moderate to prodigious rate (10–100 M$_{\odot}$ yr^{-1}). However, these estimates are highly uncertain, given the poorly constrained lensing magnification.

J1414+5446 was found serendipitously, but similar galaxies will be readily discovered in upcoming wide-area surveys such as the HSC-Wide, LSST, and WFIRST. These bright galaxies are prime targets for detailed spectroscopic studies with JWST and 30m-class telescopes, from which a more complete picture of the physical conditions of star-forming galaxies near and within the epoch of re-ionization can be formed. Furthermore, some of the more interesting properties of J1414+5446 provide a guide for future studies of re-ionization-era galaxies. First, the exceptional strength of the Ly α emission combined with the detection of a high-ionization metal line is suggestive of a population of galaxies with observable Ly α emission in the re-ionization epoch due to a hard radiation field that ionizes their local bubble (e.g. Stark et al. 2016). Second, the detection of nebular emission lines, in this case N IV, provides an alternative path to obtaining redshifts of galaxies even when the Ly α emission is fully attenuated by a neutral IGM.

ACKNOWLEDGEMENTS

We thank the anonymous referee for a careful read of the manuscript and suggestions that improved its clarity. This work is based in part on observations made with the NASA/ESA *Hubble Space Telescope*, obtained at the Space Telescope Science Institute, which is operated by the Association of Universities for Research in Astronomy, Inc., under NASA contract NAS 5-26555. These observations are associated with program GO #13762 with support provided by NASA through a grant from the Space Telescope Science Institute. Also based in part on observations made with the Spitzer Space Telescope, which is operated by the Jet Propulsion Laboratory, California Institute of Technology under a contract with NASA. Support for this work was provided by NASA through an award issued by JPL/Caltech (GO 90195). JPK acknowledges support from the ERC advanced grant LIDA. ML acknowledges CNRS and CNES for their support. Observations reported here were obtained at the MMT Observatory, a joint facility of the University of Arizona and the Smithsonian Institution. This paper used data obtained with the MODS spectrographs built with funding from NSF grant AST-9987045 and the NSF Telescope System Instrumentation Program (TSIP), with additional funds from the Ohio Board of Regents and the Ohio State University Office of Research. This paper made use of the modsIDL spectral data reduction pipeline developed in part with funds provided by NSF Grant AST-1108693. Based in part on observations obtained with MegaPrime/MegaCam, a joint project of CFHT and CEA/IRFU, at the Canada-France-Hawaii Telescope (CFHT), which is operated by the National Research Council (NRC) of Canada, the Institut National des Science de l'Univers of the Centre National de la Recherche Scientifique (CNRS) of France, and the University of Hawaii. This work is based in part on data products produced at Terapix available at the Canadian Astronomy Data Centre as part of the Canada–France–Hawaii Telescope Legacy Survey, a collaborative project of NRC and CNRS. This research has made use of the CFHTLS-ZPhots database, operated at CeSAM/LAM, Marseille, France. This research made use of Astropy, a community-developed core Python package for Astronomy (Astropy Collaboration et al. 2013). IRAF is distributed by the National Optical Astronomy Observatory, which is operated by the Association of Universities for Research in Astronomy (AURA) under a cooperative agreement with the National Science Foundation.

Facilities: CFHT (Megacam), MMT (Red Channel spectrograph), LBT (MODS1, LUCI1), Spitzer (IRAC), and *HST* (WFPC2,ACS,WFC3).

REFERENCES

Alexandroff R. et al., 2013, MNRAS, 435, 3306
Astropy Collaboration Robitaille T. P., Tollerud E. J. et al., 2013, A&A
Bayliss M. B., Rigby J. R., Sharon K., Wuyts E., Florian M., Gladders M. D., Johnson T., Oguri M., 2014, ApJ, 790, 144
Bernardi M. et al., 2003, AJ, 125, 1849
Bertin E., 2006, Stat. Challenges Mod. Astron. IV, 351, 112
Bertin E., Arnouts S., 1996, AJ, 117, 393
Bertin E., Mellier Y., Radovich M., Missonnier G., Didelon P., Morin B., 2002, Astron. Data Anal. Softw. Syst. XI, 281, 228
Bouwens R. J., et al., 2015, ApJ, 803, 34
Bowler R. A. A. et al., 2015, MNRAS, 452, 1817
Bruzual G., Charlot S., 2003, MNRAS, 344, 1000
Cabanac R. A. et al., 2007, A&A, 461, 813
Calzetti D., Kinney A. L., Storchi-Bergmann T., 1994, ApJ, 429, 582
Charlot S., Fall S. M., 1993, ApJ, 415, 580
Christensen L. et al., 2012, MNRAS, 427, 1973
Coleman G. D., Wu C. C., Weedman D. W., 1980, ApJS, 43, 393
Coupon J. et al., 2009, A&A, 500, 981
Dijkstra M., Lidz A., Wyithe J. S. B., 2007, MNRAS, 377, 1175
Ellis R. S. et al., 2013, ApJ, 763, L7
Erb D. K. et al., 2014, ApJ, 795, 33
Ferland G. J., Osterbrock D. E., 1986, ApJ, 300, 658
Foëx G., Motta V., Limousin M., Verdugo T., More A., Cabanac R., Gavazzi R., Munoz R. P., 2013, A&A, 559, A105
Fosbury R. A. E., et al., 2003, ApJ, 596, 797
Frye B., Broadhurst T., Benítez N., 2002, ApJ, 568, 558
Gronke M., 2017, A&A, 608, A139
Gronke M., Bull P., Dijkstra M., 2015, ApJ, 812, 123
Gruen D. et al., 2014, MNRAS, 442, 1507
Gwyn S. D. J., 2012, AJ, 143, 38
Hashimoto T. et al., 2017, A&A, 608, A10
Horne K., 1986, PASP, 98, 609
Ilbert O. et al., 2006, A&A, 457, 841
Jiang L. et al., 2013, ApJ, 773, 153
Jones T., Stark D. P., Ellis R. S., 2012, ApJ, 751, 51
Jullo E., Kneib J.-P., Limousin M., Elíasdóttir Á., Marshall P. J., Verdugo T., 2007, New J. Phys., 9, 447

Kashikawa N. et al., 2004, Publ. Astron. Soc. Japan, 56, 1011
Kennicutt R. C. J., 1998, Annu. Rev. Astron. Astrophys., 36, 189
Kirkpatrick J. A. et al., 2011, ApJ, 743, 125
Koekemoer A. M. et al., 2011, ApJS, 197, 36
Koekemoer A. M. et al., 2013, ApJS, 209, 3
Lidman C., Hayes M., Jones D. H., Schaerer D., Westra E., Tapken C., Meisenheimer K., Verhamme A., 2012, ApJ, 420, 1946
Loeb A., Rybicki G. B., 1999, ApJ, 524, 527
Lupton R., Blanton M. R., Fekete G., Hogg D. W., O'Mullane W., Szalay A., Wherry N., 2004, PASP, 116, 133
Madau P., Pozzetti L., Dickinson M., 1998, ApJ, 498, 106
Mainali R., Kollmeier J. A., Stark D. P., Simcoe R. A., Walth G., Newman A. B., Miller D. R., 2017, ApJ, 836, L14
McGreer I. D. et al., 2013, ApJ, 768, 105
McGreer I. D., Fan X., Jiang L., Cai Z., 2018, AJ, 155, 131
More A., Cabanac R., More S., Alard C., Limousin M., Kneib J.-P., Gavazzi R., Motta V., 2012, ApJ, 749, 38
Oke J. B., Gunn J. E., 1983, AJ, 266, 713
Ouchi M. et al., 2018, PASJ, 70, S13
Patrício V. et al., 2016, MNRAS, 456, 4191
Pirzkal N., Malhotra S., Rhoads J. E., Xu C., 2007, ApJ, 667, 49
Planck Collaboration et al., 2014a, A&A, 571, 16
Planck Collaboration et al., 2014b, A&A, 571, 29
Pogge R. W. et al., 2006, in McLean, ed., Ground-Based Airborne Instrum. Astronomy, 6269, 16
Robertson B. E., Ellis R. S., Dunlop J. S., McLure R. J., Stark D. P., 2010, Nature, 468, 49
Robertson B. E., Ellis R. S., Furlanetto S. R., Dunlop J. S., 2015, ApJL, 802, L19
Schaerer D., 2002, A&A, 382, 28
Schlegel D. J., Finkbeiner D. P., Davis M., 1998, AJ, 500, 525
Seifert W. et al., 2003, in Iye M., Moorwood A. F. M., eds., Ground-Based and Airborne Instrumentation for Astronomy II LUCIFER: A Multi-Mode NIR Instrument for the LBT, SPIE, p. 962
Shapley A. E., Steidel C. C., Pettini M., Adelberger K. L., 2003, ApJ, 588, 65
Shibuya T. et al., 2018, PASJ, 70, S14
Skrutskie M. F. et al., 2006, AJ, 131, 1163
Smit R. et al., 2017, MNRAS, 467, 3306
Songaila A., Cowie L. L., 2010, ApJ, 721, 1448
Stark D. P., 2016, ARAA, 54, 761
Stark D. P., Schenker M. A., Ellis R., Robertson B., McLure R., Dunlop J., 2013, ApJ, 763, 129
Stark D. P. et al., 2014, MNRAS, 445, 3200
Stark D. P. et al., 2015, MNRAS, 450, 1846
Stark D. P. et al., 2015, MNRAS, 454, 1393
Stark D. P. et al., 2016, MNRAS,stw2233
Vanzella E. et al., 2010, A&A, 513, A20
Venemans B. P. et al., 2005, ApJ, 431, 793
Verhamme A., Schaerer D., Atek H., Tapken C., 2008, A&A, 491, 89
Willott C. J. et al., 2013, AJ, 145, 4
Willott C. J., Carilli C. L., Wagg J., Wang R., 2015, ApJ, 807, 180
Wisotzki L. et al., 2016, A&A, 587, A98
Worseck G., Prochaska J. X., 2011, ApJ, 728, 23
Worseck G. et al., 2014, MNRAS, 445, 1745
Yang H., Wang J., Zheng Z.-Y., Malhotra S., Rhoads J. E., Infante L., 2014, ApJ, 784, 35
Yang H. et al., 2017, ApJ, 844, 171

APPENDIX A: ADDITIONAL MODS SPECTROSCOPY

The MODS1 spectroscopic observations included slits placed on interesting objects within the field of J1414+5446. These include a long slit aligned with the tangential arc T1 (masks 505919 and 523405), two slits for each of the radial arc candidates R1 and R2 (mask 510122), and cluster member galaxies selected through simple colour cuts. Specifically, the member galaxy candidates were targeted with the criteria $g - r > 1.2$ and $r - i > 0.7$ using the CFHTLS photometry. In total, these criteria select 662 objects within 6 arcmin of the BCG position to a depth of $i < 25$. We targeted 52 galaxies within $\sim$2.5 arcmin of the BCG, obtaining redshifts for 43 galaxies with $0.58 < z < 0.64$ (the BCG redshift is $z = 0.616$). A few additional galaxies that did not meet the colour criteria were also targeted on order to fill the slit masks.

The full redshift catalogue from the MODS1 observations is given in Table A1. Objects with $z = 0$ are confirmed late-type stars, while those with an empty redshift entry were not identifiable, usually due to low *S*/*N*. Typical errors on the redshifts are <20 km s^{-1}. Example MODS spectra are presented in Fig. A1.

We obtain a redshift of $z = 0.285$ for the candidate radial arc R1 from More et al. (2012), based on detections of O III 5007 and O II 3727, and a marginal detection of H α. The R1 spectrum may be contaminated by a nearby galaxy to the NW (see Fig. A2) and as such there remains some possibility that it is at higher redshift. The candidate arc R2 has a redshift of $z = 0.509$ based on O III 4959, 5007, and O II 3727. These redshifts place both of the objects in the foreground of the lensing mass, and thus they are not lensed arcs. Even with a total exposure time of $\sim$9 h, we were unable to obtain signal on the candidate tangential arc T1. We first attempted to collapse the full 14-arcsec slit into a single 1D spectrum with uniform per-pixel weights. Next, we constructed a 1D slit profile matching the profile in the *HST* images in order to assign greater weight to the brighter knots associated with the galaxy. Neither method resulted in any detectable continuum or line emission. An image of the targets in the cluster centre is presented in Fig. A2.

Table A1. Redshifts of field galaxies.

RA (J2000)	Dec. (J2000)	$i(AB)$	z	RA (J2000)	Dec. (J2000)	$i(AB)$	z
213.63864	54.80231	20.37	0.61207	213.63982	54.80292	21.09	0.62854
213.64101	54.76356	21.61	0.62484	213.64482	54.77097	17.18	0.00000
213.64774	54.80578	20.40	0.61501	213.64890	54.76526	20.82	0.60856
213.65602	54.77777	21.88	0.59960	213.65744	54.81451	21.26	0.51609
213.66525	54.78886	19.93	0.59645	213.66668	54.81920	21.41	0.61464
213.66811	54.80514	20.54	0.61257	213.66841	54.78838	19.71	0.59668
213.66989	54.80754	21.24	0.85058	213.68693	54.79591	21.11	0.62238
213.68789	54.76468	20.08	0.60376	213.69023	54.78886	20.95	0.61697
213.69038	54.80107	21.77	0.60402	213.69096	54.80299	21.75	0.61283
213.69357	54.79611	21.00	0.61429	213.69402	54.78219	23.21	0.50876
213.69470	54.78325	19.56	0.61347	213.69480	54.79008	19.83	0.62059
213.69486	54.75863	20.62	0.61276	213.69503	54.74819	21.95	0.19803
213.69573	54.82074	21.76	0.61585	213.69662	54.78430	18.32	0.61562
213.69729	54.80092	20.30	0.60472	213.69766	54.79988	21.78	0.61200
213.69860	54.80782	20.31	0.62577	213.69895	54.78682	21.15	0.60836
213.69907	54.75195	19.29	0.00000	213.69965	54.78808	20.93	0.61550
213.69966	54.75082	21.79	0.60437	213.70032	54.78400	21.64	0.28546
213.70149	54.79680	22.09	0.62181	213.70456	54.79925	22.26	0.61868
213.70540	54.78141	22.18	0.61843	213.70575	54.78055	21.49	0.59664
213.70600	54.76151	19.73	0.51899	213.70635	54.80830	21.62	0.61173
213.70646	54.78522	21.57	0.61511	213.70714	54.76068	21.65	0.60930
213.70874	54.82911	18.55	0.00000	213.71126	54.74782	21.75	0.61017
213.71588	54.74148	18.80	0.52287	213.71917	54.75171	20.90	0.56825
213.71998	54.75488	21.22	0.52187	213.72032	54.76813	21.19	0.61002
213.72506	54.74987	21.16	0.61393	213.72995	54.77044	22.08	0.61455
213.73236	54.76782	21.52	0.61254	213.73911	54.79662	21.19	0.61576
213.74338	54.79890	21.05	0.62441	213.74414	54.77551	19.72	0.61317
213.74979	54.80938	21.63	0.61607				

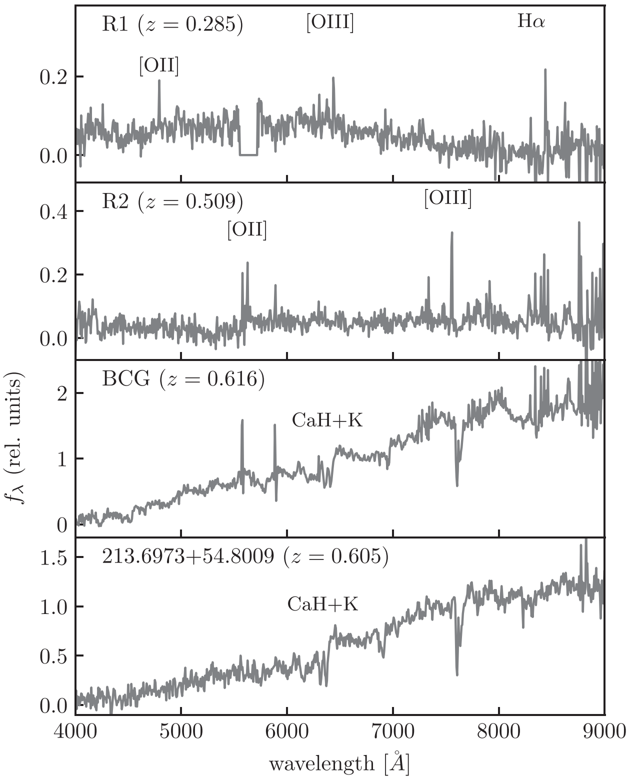

Figure A1. Spectra of galaxies in the field of J1414+5446 targeted on MODS slitmasks. Spectra of the two candidate arcs R1 and R2 are presented in the top two panels; both are star-forming galaxies with strong emission lines. The unambiguous redshifts place them in the foreground of the lensing cluster. The third panel from the top shows the BCG spectrum, and the lowest panel a randomly selected cluster member galaxy that is representative of the quality of the MODS spectra.

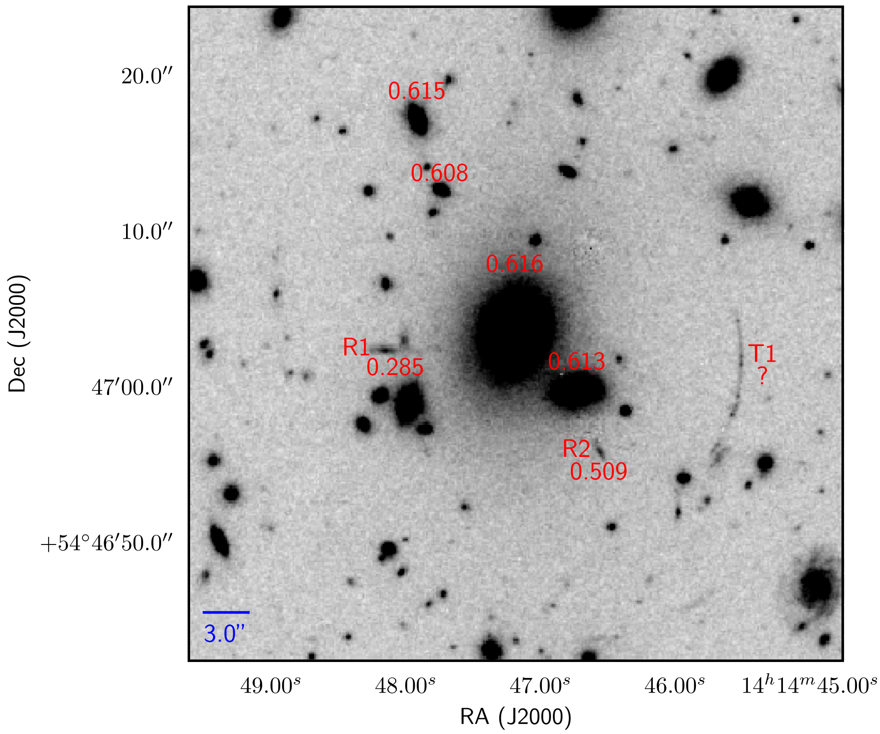

Figure A2. Central ∼20 arcsec of the lensing cluster SL2S J141447+544703 from the *HST*/WFC3 F125W image. Objects with MODS spectroscopy are labelled with their redshift just above the source, except for the candidate lensing arcs that are labelled with both their name and the redshift below the name. The data are unable to yield a redshift for the tangential arc T1. The two candidate radial arcs R1 and R2 are in the foreground of the cluster.

This paper has been typeset from a TEX/LATEX file prepared by the author.